

Virological characteristics of SARS-CoV-2 BA.2 variant

Daichi Yamasoba^{1,2,31}, Izumi Kimura^{1,31}, Hesham Nasser^{3,4,31}, Yuhei Morioka^{5,31}, Naganori Nao^{6,7,31}, Jumpei Ito^{1,31}, Keiya Uriu^{1,8,31}, Masumi Tsuda^{9,10,31}, Jiri Zahradnik^{11,31}, Kotaro Shirakawa¹², Rigel Suzuki⁵, Mai Kishimoto¹³, Yusuke Kosugi^{1,14,15}, Kouji Kobiyama¹⁶, Teppei Hara¹⁶, Mako Toyoda¹⁷, Yuri L Tanaka¹⁸, Erika P Butlertanaka¹⁸, Ryo Shimizu³, Hayato Ito⁵, Lei Wang^{9,10}, Yoshitaka Oda⁹, Yasuko Orba^{13,19}, Michihito Sasaki^{13,19}, Kayoko Nagata¹², Kumiko Yoshimatsu²⁰, Hiroyuki Asakura²¹, Mami Nagashima²¹, Kenji Sadamasu²¹, Kazuhisa Yoshimura²¹, Jin Kuramochi²², Motoaki Seki²³, Ryoji Fujiki²³, Atsushi Kaneda²³, Tadanaga Shimada²⁴, Taka-aki Nakada²⁴, Seiichiro Sakao²⁵, Takuji Suzuki²⁵, Takamasa Ueno¹⁷, Akifumi Takaori-Kondo¹², Ken J Ishii¹⁶, Gideon Schreiber¹¹, The Genotype to Phenotype Japan (G2P-Japan) Consortium, Hirofumi Sawa^{6,7,13,19}, Akatsuki Saito^{18,26,27*}, Takashi Irie^{28*}, Shinya Tanaka^{9,10*}, Keita Matsuno^{7,19,29*}, Takasuke Fukuhara^{5*}, Terumasa Ikeda^{3*}, Kei Sato^{1,8,30*}.

¹ Division of Systems Virology, Department of Infectious Disease Control, International Research Center for Infectious Diseases, The Institute of Medical Science, The University of Tokyo, Tokyo, Japan.

² Faculty of Medicine, Kobe University, Kobe, Japan.

³ Division of Molecular Virology and Genetics, Joint Research Center for Human Retrovirus infection, Kumamoto University, Kumamoto, Japan.

⁴ Department of Clinical Pathology, Faculty of Medicine, Suez Canal University, Ismailia, Egypt.

⁵ Department of Microbiology and Immunology, Graduate School of Medicine, Hokkaido University, Sapporo, Japan.

⁶ Division of International Research Promotion, International Institute for Zoonosis Control, Hokkaido University, Sapporo, Japan.

⁷ One Health Research Center, Hokkaido University, Sapporo, Japan.

⁸ Graduate School of Medicine, The University of Tokyo, Tokyo, Japan.

⁹ Department of Cancer Pathology, Faculty of Medicine, Hokkaido University, Sapporo, Japan.

¹⁰ Institute for Chemical Reaction Design and Discovery (WPI-ICReDD), Hokkaido University, Sapporo, Japan.

¹¹ Department of Biomolecular Sciences, Weizmann Institute of Science, Rehovot, Israel.

¹² Department of Hematology and Oncology, Graduate School of Medicine, Kyoto University, Kyoto, Japan.

¹³ Division of Molecular Pathobiology, International Institute for Zoonosis Control, Hokkaido University, Sapporo, Japan.

- 41 ¹⁴ Laboratory of Systems Virology, Institute for Frontier Life and Medical
42 Sciences, Kyoto University, Kyoto, Japan.
- 43 ¹⁵ Graduate School of Pharmaceutical Sciences, Kyoto University, Kyoto, Japan.
- 44 ¹⁶ Division of Vaccine Science, Department of Microbiology and Immunology,
45 The Institute of Medical Science, The University of Tokyo, Tokyo, Japan.
- 46 ¹⁷ Division of Infection and immunity, Joint Research Center for Human
47 Retrovirus infection, Kumamoto University, Kumamoto, Japan
- 48 ¹⁸ Department of Veterinary Science, Faculty of Agriculture, University of
49 Miyazaki, Miyazaki, Japan.
- 50 ¹⁹ International Collaboration Unit, International Institute for Zoonosis Control,
51 Hokkaido University, Sapporo, Japan.
- 52 ²⁰ Institute for Genetic Medicine, Hokkaido University, Sapporo, Japan.
- 53 ²¹ Tokyo Metropolitan Institute of Public Health, Tokyo, Japan.
- 54 ²² Kuramochi Clinic Interpark, Utsunomiya, Japan.
- 55 ²³ Department of Molecular Oncology, Graduate School of Medicine, Chiba
56 University, Chiba, Japan.
- 57 ²⁴ Department of Emergency and Critical Care Medicine, Graduate School of
58 Medicine, Chiba University, Chiba, Japan.
- 59 ²⁵ Department of Respiriology, Graduate School of Medicine, Chiba University,
60 Chiba, Japan.
- 61 ²⁶ Center for Animal Disease Control, University of Miyazaki, Miyazaki, Japan.
- 62 ²⁷ Graduate School of Medicine and Veterinary Medicine, University of Miyazaki,
63 Miyazaki, Japan.
- 64 ²⁸ Institute of Biomedical and Health Sciences, Hiroshima University, Hiroshima,
65 Japan.
- 66 ²⁹ Division of Risk Analysis and Management, International Institute for Zoonosis
67 Control, Hokkaido University, Sapporo, Japan.
- 68 ³⁰ CREST, Japan Science and Technology Agency, Saitama, Japan.
- 69 ³¹ These authors contributed equally: Izumi Kimura, Daichi Yamasoba, Hesham
70 Nasser, Yuhei Morioka, Naganori Nao, Jumpei Ito, Keiya Uriu, Masumi Tsuda,
71 Jiri Zahradnik.
- 72
- 73 *Corresponding authors:
74 sakatsuki@cc.miyazaki-u.ac.jp (Akatsuki Saito);
75 tirie@hiroshima-u.ac.jp (Takashi Irie);
76 tanaka@med.hokudai.ac.jp (Shinya Tanaka);
77 matsuk@czc.hokudai.ac.jp (Keita Matsuno);
78 fukut@pop.med.hokudai.ac.jp (Takasuke Fukuhara);
79 ikedat@kumamoto-u.ac.jp (Terumasa Ikeda);
80 KeiSato@g.ecc.u-tokyo.ac.jp (Kei Sato)
- 81

82 **Keywords:**

83 SARS-CoV-2; COVID-19; Omicron; BA.2; BA.1; B.1.1.529; pathogenicity;
84 fusogenicity; transmissibility

85 **Abstract**

86 Soon after the emergence and global spread of a new severe acute respiratory
 87 syndrome coronavirus 2 (SARS-CoV-2) Omicron lineage, BA.1 (ref^{1,2}), another
 88 Omicron lineage, BA.2, has initiated outcompeting BA.1. Statistical analysis
 89 shows that the effective reproduction number of BA.2 is 1.4-fold higher than that
 90 of BA.1. Neutralisation experiments show that the vaccine-induced humoral
 91 immunity fails to function against BA.2 like BA.1, and notably, the antigenicity of
 92 BA.2 is different from BA.1. Cell culture experiments show that BA.2 is more
 93 replicative in human nasal epithelial cells and more fusogenic than BA.1.
 94 Furthermore, infection experiments using hamsters show that BA.2 is more
 95 pathogenic than BA.1. Our multiscale investigations suggest that the risk of BA.2
 96 for global health is potentially higher than that of BA.1.

97 Introduction

98 Virological characteristics of newly emerging SARS-CoV-2 variants, such as
99 transmissibility, pathogenicity and resistance to the vaccine-induced immunity
100 and antiviral drugs, is an urgent global health concern. In February 2022, the
101 Omicron variant (B.1.1.529 and BA lineages) spreads worldwide and represents
102 the most recently recognised variant of concern². Omicron was first reported
103 from South Africa at the end of November 2021¹. Then, a variant of Omicron, the
104 BA.1 lineage, has rapidly spread worldwide and outcompeted other variants
105 such as Delta.

106 As of February 2022, another variant of Omicron, the BA.2 lineage, has
107 detected in multiple countries such as Denmark and UK³. Notably, BA.2 has
108 initiated outcompeting BA.1³, suggesting that BA.2 is more transmissible than
109 BA.1.

110 In a few months since the emergence of BA.1, we and others revealed
111 the virological characteristics of BA.1⁴⁻¹⁹. For instance, BA.1 is highly resistant to
112 the vaccine-induced humoral immunity and antiviral drugs^{4-11,16-19}. Also, the
113 spike (S) protein of BA.1 is less efficiently cleaved by furin and less fusogenic
114 than those of Delta and an ancestral SARS-CoV-2 belonging to the B.1.1
115 lineage^{11,12}. Further, the pathogenicity of BA.1 is attenuated when compared to
116 Delta and an ancestral B.1.1 virus¹²⁻¹⁴. However, the virological characteristics of
117 BA.2 remains unaddressed.

118

119 Phylogenetic and epidemic dynamics of BA.2

120 As of February 2022, Omicron is classified into three main lineages, BA.1, BA.2,
121 BA.3, and a sublineage of BA.1, BA.1.1, which harbours the R346K substitution
122 in S (**Fig. 1a**). Although these lineages are monophyletic, their sequences have
123 been greatly diversified. For example, BA.1 differs from BA.2 by 50 amino acids,
124 which is approximately twice as much as the numbers of amino acid differences
125 between four VOCs (Alpha, Beta, Gamma and Delta) and Wuhan-Hu-1, a
126 prototypic SARS-CoV-2 isolate (**Fig. 1b**). Phylodynamics analysis suggests that
127 BA.1 emerged first, followed by BA.2 and BA.3 (**Extended Data Fig. 1**). In
128 addition to BA.1, the earlier strains of BA.2, BA.3, and BA.1.1 were isolated from
129 Gauteng Province, South Africa, the place of the earliest Omicron (BA.1)
130 epidemic (**Extended Data Fig. 1**)²⁰. These results suggest that the remarkable
131 diversification of Omicron occurred in Gauteng Province and all Omicron
132 lineages emerged there.

133 Although BA.1 spread worldwide earlier than BA.2, the lineage
134 frequency of BA.2 increased and exceeded that of BA.1 since January 2022 in
135 multiple countries, such as Philippines, India, Denmark, Singapore, Austria, and
136 South Africa (**Fig. 1c and Extended Data Fig. 2**). To quantify the growth
137 advantage of BA.2 in the human population, we constructed a Bayesian model

138 representing the epidemic dynamics of SARS-CoV-2 lineages. This hierarchical
139 model can estimate the global average of the relative effective reproduction
140 numbers of viral lineages (**Fig. 1d**) as well as those in each country (**Extended**
141 **Data Fig. 2**). The effective reproduction number of BA.2 is 1.40-fold higher than
142 that of BA.1 on average in the world [95% confidence interval (CI), 1.29–1.52;
143 **Fig. 1d**]. Furthermore, the effective reproduction number of BA.2 was even
144 higher than that of BA.1.1, which spread more rapidly than BA.1 in several
145 countries such as the UK and USA (**Fig. 1d and Extended Data Fig. 2d**). These
146 results suggest that the BA.2 epidemic will more expand around the world,
147 raising the importance of elucidating virological features of BA.2 in depth.

148

149 **Immune resistance of BA.2**

150 Since the sequence of BA.2, particularly in S protein, is substantially different
151 from that of BA.1 (**Fig. 1b and Fig. 2a**), it is reasonable to assume that the
152 virological properties of BA.2, such as immune resistance and pathogenicity, are
153 different from those of BA.1. To reveal the virological features of BA.2, we set
154 out to perform neutralisation assay using pseudoviruses and the neutralising
155 antibodies elicited by vaccination. Consistent with recent studies^{4-11,16-19}, BA.1 is
156 highly resistant to the antisera elicited by mRNA-1273 and ChAdOx1 vaccines
157 (**Fig. 2b,c**). Similar to BA.1, BA.2 was also highly resistant to the
158 vaccine-induced antisera (**Fig. 2b,c**). Also, BA.2 was almost completely
159 resistant to two therapeutic monoclonal antibodies, Casirivimab and Imdevimab,
160 and was 35-fold more resistant to another therapeutic antibody, Sotrovimab,
161 when compared to the ancestral D614G-bearing B.1.1 virus (**Fig. 2d**). Moreover,
162 both BA.1 and BA.2 were highly resistant to the convalescent sera who had
163 infected with early pandemic virus (before May 2020; **Fig. 2e**), Alpha (**Extended**
164 **data Fig. 3a**) and Delta (**Extended data Fig. 3b**). These data suggest that,
165 similar to BA.1, BA.2 is highly resistant to the antisera induced by vaccination
166 and infection with other SARS-CoV-2 variants as well as three antiviral
167 therapeutic antibodies.

168 We then tested the 17 sera infected with BA.1: 13 convalescents were
169 fully vaccinated (2 shots), 1 convalescent was 1-dose vaccinated, and 3
170 convalescents were not vaccinated. BA.1 convalescent sera exhibited the
171 strongest antiviral effect against BA.1 (**Fig. 2f**). Although BA.2 was 1.4-fold more
172 resistant to the BA.1-infected sera than BA.1, there was no statistical difference
173 (**Fig. 2f**; $P=0.091$ by Wilcoxon signed-rank test). Importantly, the BA.1
174 convalescent sera with full vaccination exhibited significantly stronger antiviral
175 effects against all variants tested than unvaccinated or 1-dose vaccinated
176 convalescents (**Extended Data Fig. 3c**).

177 To address the possibility that the BA.1-induced humoral immunity is
178 less effective against BA.2, we used the convalescent sera obtained from

179 infected hamsters at 16 days postinfection (d.p.i.). Similar to the results of
180 convalescent human sera (**Fig. 2e** and **Extended Data Fig. 2b**), both BA.1 and
181 BA.2 exhibited pronounced resistances against B.1.1- and Delta-infected
182 convalescent hamster sera (**Fig. 2g** and **Extended Data Fig. 3d**). Interestingly,
183 BA.2 was significantly (2.9-fold) more resistant to BA.1-infected convalescent
184 hamster sera than BA.1 (**Fig. 2g**). To further verify the resistance of BA.2
185 against BA.1-induced immunity, mice were immunised with the cells expressing
186 the S proteins of ancestral B.1.1 and BA.1 and obtained murine antisera. Again,
187 the neutralisation assay using murine sera showed that BA.2 is more
188 significantly (6.4-fold) resistant to the BA.1 S-immunised sera than BA.1 (**Fig.**
189 **2h**). These findings suggest that BA.1-induced humoral immunity is less
190 effective against BA.2.

191

192 **Virological features of BA.2 in vitro**

193 To investigate the virological characteristics of BA.2, we generated chimeric
194 recombinant SARS-CoV-2 that expresses GFP and harbours the S gene of
195 ancestral B.1.1, Delta, BA.1 and BA.2 by reverse genetics (**Extended Data Fig.**
196 **4**)²¹. Although the growth of BA.1 and BA.2 was comparable in
197 VeroE6/TMPRSS2 cells, BA.2 was more replicative than BA.1 in Calu-3 cells
198 and primary human nasal epithelial cells (**Fig. 3a**). Notably, the morphology of
199 infected cells was different; BA.2 formed significantly (1.52-fold) larger syncytia
200 than BA.1 (**Fig. 3b** and **Extended Data Fig. 5a**). Whereas the plaque size in
201 VeroE6/TMPRSS2 cells infected with BA.1 and BA.2 was significantly smaller
202 than those of cells infected with B.1.1, the plaques formed by BA.2 infection are
203 significantly (1.27-fold) larger than those by BA.1 infection (**Fig. 3c** and
204 **Extended Data Fig. 5b**). Moreover, the coculture of S-expressing cells with
205 HEK293-ACE2/TMPRSS2 cells showed that BA.2 S induces significantly
206 (2.9-fold) larger multinuclear syncytia formation when compared to BA.1 S
207 (**Extended Data Fig. 5c**). These data suggest that BA.2 is more fusogenic than
208 BA.1. To further address this possibility, we analysed the fusogenicity of the S
209 proteins of BA.2 S by a cell-based fusion assay^{12,22,23}. The expression level of
210 BA.2 S on the cell surface was significantly lower than that of BA.1 S (**Extended**
211 **Data Fig. 6a**). Nevertheless, our fusion assay using VeroE6/TMPRSS2 cells and
212 Calu-3 cells showed that BA.2 S is significantly more fusogenic than BA.1 S (**Fig.**
213 **3d**). We then analysed the binding affinity of BA.2 S receptor binding domain
214 (RBD) to ACE2 by a yeast surface display assay^{16,22,24}. Although the binding
215 affinity of BA.1 S RBD to ACE2 is controversial^{11,15-17,25,26}, our yeast surface
216 display showed that the binding affinity of the RBD of BA.1 and BA.2 is
217 comparable (**Extended Data Fig. 6b**).

218 Because we have proposed that the SARS-CoV-2 S-mediated
219 fusogenicity is closely associated with the efficacy of S1/S2 cleavage^{12,23}, we

220 hypothesized that BA.2 S is more efficiently cleaved than BA.1 S. However, an
221 western blotting analysis showed that BA.2 S is less cleaved than BA.1 S (**Fig.**
222 **3e**), suggesting that BA.2 S exhibits a higher fusogenicity independently of
223 S1/S2 cleavage.

224 We have recently revealed that BA.1 poorly utilizes TMPRSS2 for the
225 infection¹¹. To analyse the TMPRSS2 usage by BA.2 S, we performed
226 cell-based fusion assay using 293-ACE2 cells with or without TMPRSS2
227 expression. We verified that 293-ACE2 cells do not express endogenous
228 TMPRSS2 on the cell surface (**Extended Data Fig. 6c**). As shown in **Fig. 3f**, the
229 fusogenicity of BA.2 S was significantly higher in both cell lines than that of BA.1.
230 However, although BA.2 S was less fusogenic than B.1.1 S in 293-ACE2 cells,
231 the fusogenicity of BA.2 S and B.1.1 S was comparable in 293-ACE2/TMPRSS2
232 cells (**Fig. 3f**). These results suggest that the relatively higher fusogenicity of
233 BA.2 is dependent on TMPRSS2 expression on the surface of target cells. To
234 further assess whether the TMPRSS2-dependent infection enhancement was
235 also observed in cell-free virus, we inoculated pseudoviruses into 293-ACE2
236 cells and 293-ACE2/TMPRSS2 cells. Although the infectivity of B.1.1 and Delta
237 was 15.3-fold and 24.6-fold increased by TMPRSS2 expression, respectively,
238 the TMPRSS2 expression on the target cells did not affect the infectivity of both
239 BA.1 and BA.2 (**Fig. 3g**). These results suggest that TMPRSS2 does not affect
240 the infectivity of cell-free BA.2 virus. However, although the growth of BA.2 and
241 BA.1 was comparable in 293-ACE2 cells, BA.2 was more replicative than BA.1
242 in 293-ACE2/TMPRSS2 cells (**Fig. 3h**). Overall, our data suggest that BA.2 is
243 more fusogenic and replicative than BA.1 in a TMPRSS2-dependent fashion.

245 **Virological features of BA.2 in vivo**

246 To investigate the dynamics of viral replication of BA.2 *in vivo*, we conducted
247 hamster infection experiments. Consistent with our recent study¹², B.1.1-infected
248 hamsters exhibited decreased body weight and respiratory disorders that are
249 reflected by two surrogate markers for bronchoconstriction or airway obstruction,
250 enhanced pause (Penh) and the ratio of time to peak expiratory flow relative to
251 the total expiratory time (Rpef), and subcutaneous oxygen saturation (SpO₂),
252 whereas BA.1-infected hamsters exhibited no or weak disorders (**Fig. 4a**).
253 Notably, all parameters routinely measured, including body weight, Penh, Rpef
254 and SpO₂, of BA.2-infected hamsters were significantly different from uninfected
255 and BA.1-infected hamsters, and these values were comparable to those of
256 B.1.1-infected hamsters (**Fig. 4a**). These data suggest that BA.2 is more
257 pathogenic than BA.1.

258 To analyse viral spread in the respiratory organs of infected hamsters,
259 viral RNA load and nucleocapside (N) expression were assessed by RT-qPCR
260 of viral RNA and immunohistochemistry (IHC), respectively. As shown in **Fig. 4b**,

viral RNA loads in the two lung regions, hilum and periphery, of BA.2-infected hamsters were significantly higher than those of BA.1-infected hamsters. In the lung periphery, the viral RNA load of BA.2 was significantly higher than that of B.1.1, and the viral RNA load of BA.2 at 1 d.p.i. was 11-fold and 9.3-fold higher than those of B.1.1 and BA.1 at the same timepoint, respectively (**Fig. 4b**). To address the possibility that BA.2 more efficiently spreads than BA.1, we investigated the positivity for N protein in the trachea and lung area close to the hilum. At 1 d.p.i., N protein was detectable in the lower tracheal epithelium in all infected hamsters, and particularly, was clearly detectable in the middle part of trachea in BA.2-infected hamsters (**Extended Data Fig. 7a**). The positivity of N protein was observed in both bronchial and bronchiolar epithelium in all infected lungs (**Extended Data Fig. 7b**). Notably, alveolar positivities were observed in B.1.1- and BA.2-infected lungs but not in BA.1-infected lungs (**Extended Data Fig. 7b**). Morphometry showed that the percentage of N-positive cells in BA.2-infected lungs is significantly higher than that of BA.1-infected lungs and peaked at 3 d.p.i. (**Fig. 4c** and **Extended Data Fig. 7c**). On the other hand, at 3 d.p.i., the percentage of N-positive cells in the bronchus/bronchioles of BA.2-infected hamsters was 5.4-fold lower than that of BA.1-infected hamsters (**Fig. 4d**). At 5 d.p.i., N protein was almost disappeared in BA.1-infected lungs, whereas alveolar staining was still detectable in B.1.1- and BA.2-infected lungs (**Fig. 4c** and **Extended Data Fig. 7c**). These data suggest that BA.2 is more rapidly and efficiently spread in the lung tissues than BA.1.

Pathogenicity of BA.2

To investigate the pathogenicity of BA.2, the right lungs of infected hamsters were collected at 1, 3, and 5 d.p.i. and used them for haematoxylin and eosin (H&E) staining and histopathological analysis^{12,23}. All histopathological parameters including bronchitis/bronchiolitis, haemorrhage, alveolar damage, and the levels of type II pneumocytes, of BA.2-infected hamsters were significantly higher than those in BA.1 (**Fig 4e** and **Extended Data Fig. 8a**). The score indicating haemorrhage including congestive edema of BA.2 was significantly higher than that of B.1.1 (**Fig. 4e**). As shown in our previous studies^{12,23}, hyperplastic large type II pneumocytes suggesting the severity of inflammation were observed in all infected hamsters at 5 d.p.i., and particularly, the area of large type II pneumocytes in BA.2-infected hamsters was significantly larger than those in B.1.1- and BA.1-infected hamsters (**Fig. 4e**). Total histology score of BA.2 was significantly higher than that of BA.1 (**Fig. 4e**). Furthermore, in the BA.2- and B.1.1-infected lungs, the inflammation with type II alveolar pneumocyte hyperplasia was found in each lobe especially frontal/upper and accessory lobes (**Extended Data Fig. 8b**).

301 Discussion

302 Although BA.2 is considered as an Omicron variant, its genomic sequence is
303 heavily different from BA.1, which suggests that the virological characteristics of
304 BA.2 is different from that of BA.1. Here, we elucidated the virological
305 characteristics of BA.2, such as its higher effective reproduction number, higher
306 fusogenicity, higher pathogenicity when compared to BA.1. Moreover, we
307 demonstrated that BA.2 is resistant to the BA.1-induced humoral immunity. Our
308 data indicate that BA.2 is virologically different from BA.1 and raise a proposal
309 that BA.2 should be given a letter of the Greek alphabet and be distinguished
310 from BA.1, a commonly recognized Omicron variant.

311 We showed evidence suggesting that BA.2 is virologically different and
312 distinguishable from BA.1. First, by using the two different types of antisera that
313 were obtained from experimental animals, convalescent hamsters infected with
314 BA.1 and mice immunized with the BA.1 S protein, we showed that the
315 resistance of BA.2 to the BA.1-induced humoral immunity. Our results indicate
316 that the antigenicity of BA.2 is different from BA.1. Although similar tendency
317 was observed in human samples as well, a statistically significant difference was
318 not observed probably because a relatively lower number of vaccine-naïve
319 individuals who were infected with BA.1 (3 unvaccinated donors and a 1-dose
320 vaccinated donor) were tested in the present study. The effect of BA.1-induced
321 humoral immunity against BA.2 in humans should deeply be verified in the future
322 investigation.

323 Second, the higher fusogenicity of BA.2 S is a pronounced
324 characteristics in in vitro experiments. We have demonstrated that Delta S is
325 highly fusogenic than BA.1 S and B.1.1 S, and we considered that the higher
326 fusogenicity is attributed to the higher efficacy of S cleavage^{11,12,23,27}. However,
327 BA.2 S exhibited higher fusogenicity than BA.1 S without the increase of S
328 cleavage efficacy. In recent studies^{12,23}, we have proposed that the fusogenicity
329 of SARS-CoV-2 variant is closely related to its pathogenicity. This hypothesis is
330 further supported by the observations in BA.2 in the present study. However,
331 unlike Delta, the higher fusogenicity of BA.2 appears to be not attributed to the
332 higher efficacy of S cleavage^{11,12,23,27}. Moreover, although TMPRSS2 increased
333 the efficacies of both cell-cell fusion²³ and cell-free infection mediated by B.1.1 S
334 and Delta S, TMPRSS2 increased the efficacy of BA.2 S-mediated cell-cell
335 fusion but did not affect that of BA.2 S-mediated cell-free infection. These
336 observations suggest that TMPRSS2 contributes to the cell-cell fusion and
337 cell-free infection mediated by BA.2 S with different mechanisms of action.

338 Third, it would be most critical for global health that BA.2 exhibits higher
339 pathogenicity than BA.1. Although clinical researches on the BA.2 pathogenicity
340 are needed, our investigations using a hamster model showed that the
341 pathogenicity of BA.2 is similar to that of an ancestral B.1.1 and higher than that

342 of BA.1. More importantly, the viral RNA load in the lung periphery and
 343 histopathological disorders of BA.2 were more severe than those of BA.1 and
 344 even B.1.1. Together with a higher effective reproduction number and
 345 pronounced immune resistance of BA.2, it is evident that the spread of BA.2 can
 346 be a serious issue for global health in the near future.

347 In summary, our data suggest the possibility that BA.2 would be the
 348 most concerned variant to global health. Currently, both BA.2 and BA.1 are
 349 recognised together as Omicron and these are almost undistinguishable. Based
 350 on our findings, we propose that BA.2 should be recognised as a unique variant
 351 of concern, and this SARS-CoV-2 variant should be monitored in depth.

352 **Methods**

353

354 **Ethics statement**

355 All experiments with hamsters were performed in accordance with the Science
356 Council of Japan's Guidelines for the Proper Conduct of Animal Experiments.
357 The protocols were approved by the Institutional Animal Care and Use
358 Committee of National University Corporation Hokkaido University (approval ID:
359 20-0123 and 20-0060). All experiments with mice were also performed in
360 accordance with the Science Council of Japan's Guidelines for the Proper
361 Conduct of Animal Experiments. The protocols were approved by the
362 Institutional Animal Experiment Committee of The Institute of Medical Science,
363 The University of Tokyo (approval ID: PA21-39). All protocols involving
364 specimens from human subjects recruited at Kyoto University, Kuramochi Clinic
365 Interpark and Chiba University were reviewed and approved by the Institutional
366 Review Boards of Kyoto University (approval ID: G1309), Kuramochi Clinic
367 Interpark (approval ID: G2021-004) and Chiba University (approval ID:
368 HS202103-03). All human subjects provided written informed consent. All
369 protocols for the use of human specimens were reviewed and approved by the
370 Institutional Review Boards of The Institute of Medical Science, The University of
371 Tokyo (approval IDs: 2021-1-0416 and 2021-18-0617), Kyoto University
372 (approval ID: G0697), Kumamoto University (approval IDs: 2066 and 2074), and
373 University of Miyazaki (approval ID: O-1021).

374

375 **Human sera collection**

376 Vaccine sera were collected from sixteen vaccinees four weeks after the second
377 vaccination with mRNA-1273 (Moderna) (average age: 27, range: 20-47, 38%
378 male). The sera obtained from nine vaccinees 10-25 d after the second
379 vaccination with ChAdOx1 (Oxford-AstraZeneca) (average age: 45, range:
380 35-54, 67% male) were purchased from BioIVT. The detail of vaccine sera is
381 summarized in **Supplementary Table 1**.

382 Convalescent sera were collected from vaccine-naive individuals who
383 had infected with Alpha variant (n=8; average age: 41, range: 21-57, 63% male)
384 and Delta variant (n=15; average age: 51, range: 22-67, 80% male).
385 Convalescent sera of BA.1-infected individuals (n=17; average age: 39, range:
386 20-65, 47% male, 76% received the second vaccination) were also collected. To
387 determine the SARS-CoV-2 variants infected, salivas were collected from
388 COVID-19 patients during onset and RNA was extracted using a QIAamp viral
389 RNA mini kit (Qiagen, Cat# 52906) according to the manufacturer's protocol. To
390 determine Alpha and Delta variants, viral genome sequencing was performed as
391 previously described¹¹. For the detail, see "Viral genome sequencing" section
392 below. To determine the BA.1 variant, mutation-targeting RT-qPCR was

performed. To detect the S E484A substitution (common in all Omicron variants including BA.1 and BA.2), a set of primer/probe E484A (SARS-CoV-2) (Takara, Cat# RC322A) was used. To detect the S R214EPE insertion (specific for B.1.1.529 and BA.1, undetectable in BA.2), a hand-made protocol was used with the following primers and probe: Omi_ins214s-F1, TTC TAA GCA CAC GCC TAT TAT AGT GC; Omi_ins214s-R1, TAA AGC CGA AAA ACC CTG AGG; and Omi_ins214s, FAM-TGA GCC AGA AGA TC-MGB. The twelve convalescent sera during early pandemic (until May 2020) (average age: 71, range: 52-92, 8% male) were purchased from RayBiotech. Sera were inactivated at 56°C for 30 min and stored at -80°C until use. The detail of convalescent sera is summarized in **Supplementary Table 2**.

Viral genome sequencing

Viral genome sequencing was performed as previously described^{11,12,22,23} with some modifications. Briefly, the sequences of the working viruses were verified by viral RNA-sequencing analysis. Viral RNA was extracted using QIAamp viral RNA mini kit (Qiagen, Cat# 52906). The sequencing library for total RNA-sequencing was prepared using NEB Next Ultra RNA Library Prep Kit for Illumina (New England Biolabs, Cat# E7530). Paired-end, 76-bp sequencing was performed using MiSeq (Illumina) with MiSeq reagent kit v3 (Illumina, Cat# MS-102-3001). Sequencing reads were trimmed using fastp v0.21.0²⁸ and subsequently mapped to the viral genome sequences of a lineage A isolate (strain WK-521; GISAID ID: EPI_ISL_408667)²⁹ using BWA-MEM v0.7.17³⁰. Variant calling, filtering, and annotation were performed using SAMtools v1.9³¹ and snpEff v5.0e³².

Phylogenetic and comparative genome analyses

To construct a maximum likelihood tree of the Omicron lineages (BA.1, BA.1.1, BA.2, and BA.3) sampled from South Africa, the genome sequence data of SARS-CoV-2 and its metadata were downloaded from the GISAID database (<https://www.gisaid.org/>) on January 26, 2022. We excluded the data of viral strains with the following features from the analysis: i) lacking the collection date information; ii) sampled from animals other than humans; iii) having the flag of low coverage sequencing; or iv) having >2% of undetermined nucleotide characters. All the BA.2 and BA.3 sequences and 200 randomly sampled BA.1 (including 20 BA.1.1) sequences were used for the tree construction in addition to an outgroup sequence, EPI_ISL_466615, the oldest isolate of B.1.1 in the UK. The viral genome sequences were mapped to the reference sequence of Wuhan-Hu-1 (GenBank accession no.: NC_045512.2) using minimap2 v2.17³³ and subsequently converted to the multiple sequence alignment according to the GISAID phylogenetic analysis pipeline

(<https://github.com/roblanf/sarscov2phylo>). The alignment sites corresponding to the 1–265 and 29674–29903 positions in the reference genome were masked (i.e., converted to NNN). The alignment sites with >50% sequences having a gap or undetermined/ambiguous nucleotide were trimmed using trimAl v1.2³⁴. The phylogenetic tree construction was performed by a two-step protocol: i) The first tree was constructed; ii) tips with a longer external branch (Z score > 4) were removed from the dataset; iii) and the final tree was constructed. The tree reconstruction was performed by RAxML v8.2.12³⁵ under the GTRCAT substitution model. Node support value was calculated by 100-times of bootstrap analysis.

We performed phylodynamics analysis of Omicron lineages (BA.1, BA.1.1, BA.2 and BA.3) sampled from South Africa as below. The SARS-CoV-2 genome sequence dataset used above was split into each Omicron lineage. As an outgroup sequence, the oldest BA.2 (GISAID ID: EPI_ISL_8128463) was added to the BA.1 and BA.3 datasets, and the oldest BA.3 (GISAID ID: EPI_ISL_8616600) was added to the BA.2 dataset. The multiple sequence alignment was constructed as the procedures described above. A time-calibrated tree of each lineage was constructed by BEAST2 v.2.6.6³⁶. The HKY model³⁷ with the four categories of discrete gamma rate variation was selected as a nucleotide substitution model. A relaxed molecular clock modelled by a log-normal distribution was selected. The exponential growth coalescent model was used. For BA.1, BA.2, and BA.3 datasets, nineteen, four, and three independent chains of Markov chain Monte Carlo (MCMC) were respectively run with 2,000,000 warmup and 18,000,000 sampling iterations. We confirmed that the effective sampling sizes for all parameters were greater than 200, indicating the MCMC runs were successfully convergent. The maximum credible trees with common ancestor heights are shown in **Extended Data Fig. 1**.

The number of amino acid differences (including nonsynonymous substitutions, insertions, and deletions) between SARS-CoV-2 lineages was defined as below. Information on amino acid differences of each viral strain compared with the reference sequence of Wuhan-Hu-1 (GenBank accession no.: NC_045512.2) was extracted from the GISAID metadata (downloaded on January 26, 2022). In each viral lineage, the amino acid differences that were present in >10% sequences were extracted and subsequently counted. For the comparison of BA.1 and BA.2, the set of the symmetric difference of the amino acid differences compared with the reference was determined and subsequently counted.

Modelling the epidemic dynamics of SARS-CoV-2 lineages

To quantify the spread speed of each SARS-CoV-2 lineage in the human population, we estimated the relative effective reproduction number of each viral

lineage according to the epidemic dynamics calculated on the basis of viral genomic surveillance data. The data were downloaded from the GISAID database (<https://www.gisaid.org/>) on February 1, 2022. We excluded the data of viral strains with the following features from the analysis: i) lacking the collection date information; ii) sampled from animals other than humans; or iii) sampled by quarantine. We analysed the datasets of the eleven countries with >100 BA.2 sequences (Austria, Denmark, Germany, India, Israel, Philippines, Singapore, South Africa, Sweden, the UK, and the USA) (**Fig. 1 and Extended Data Fig. 2**). The dynamics of BA.1, BA.1.1, BA.2, and Delta (B.1.617.2 and AY lineages) in each country from October 1, 2021, to January 25, 2022, were analysed. The number of viral sequences of each viral lineage collected on each day in each country was counted. Finally, we constructed the L (lineage) × C (country) × T (time) = 4 × 11 × 117 shaped array, which comprises the count of each viral lineage in each country in each day. This array was used as input data for the statistical model described below.

We constructed a Bayesian hierarchical model to represent the relative lineage growth dynamics with a multinomial logistic regression. The mathematical theory underlying the model is described in detail elsewhere^{38,39}, and this model is basically similar to the one used in our previous study¹². In the present study, we incorporated a hierarchical structure into the slope parameter over time, which enable us to estimate the global average of the relative effective reproduction number of each viral lineage as well as that in each country. Arrays in the model index over one or more indices: L = 4 viral lineages l ; C = 11 countries c ; and T = 117 days t . The model is:

$$\begin{aligned}\beta_{lc} &\sim \text{Student_t}(6, \beta_l, \sigma_l) \\ \mu_{lct} &= \alpha_{lc} + \beta_{lc}t \\ \theta_{ct} &= \text{softmax}(\mu_{ct}) \\ y_{lct} &\sim \text{Multinomial}\left(\sum_l y_{lct}, \theta_{ct}\right)\end{aligned}$$

The explanatory variable is time t , and the outcome variable is y_{lct} , which represents the count of viral lineage l in country c at time t . The slope parameter of lineage l in country c , β_{lc} , is generated from a student's t distribution with the hyper parameters of the mean β_l and the standard deviation σ_l . As the distribution generating β_{lc} , we used a student's t distribution with six degrees of freedom instead of a normal distribution to reduce the effects of outlier values of β_{lc} . In the model, the linear estimator μ_{ct} , consisting of the intercept α_c and the slope β_c , is converted to the simplex θ_{ct} , which represents the probability of occurrence of each viral lineage at time t in country c , by the softmax link function defined as:

$$\text{softmax}(x) = \frac{\exp(x)}{\sum_i \exp(x_i)}$$

509 y_{lct} is generated from θ_{ct} and the total count of all lineages at t in country c
 510 according to a multinomial distribution.

511 The relative effective reproduction number of each viral lineage in each
 512 county (r_{lc}) was calculated according to the slope parameter β_{lc} as:

$$r_{lc} = \exp(\gamma\beta_{lc})$$

513 where γ is the average viral generation time (2.1 day)
 514 ([http://sonorouschocolate.com/covid19/index.php?title=Estimating_Generation_](http://sonorouschocolate.com/covid19/index.php?title=Estimating_Generation_Time_Of_Omicron)
 515 [Time_Of_Omicron](http://sonorouschocolate.com/covid19/index.php?title=Estimating_Generation_Time_Of_Omicron)). Similarly, the global average of the relative effective
 516 reproduction number of each viral lineage was calculated according to the slope
 517 hyper parameter β_l as:

$$r_l = \exp(\gamma\beta_l)$$

518 For the parameter estimation, the intercept and slope parameters of the BA.1
 519 variant were fixed at 0. Consequently, the relative effective reproduction number
 520 of BA.1 was fixed at 1, and those of the respective lineages were estimated
 521 relative to that of BA.1.

522 Parameter estimation was performed by MCMC implemented in
 523 CmdStan v2.28.1 (<https://mc-stan.org>) with cmdstanr v0.4.0
 524 (<https://mc-stan.org/cmdstanr/>). Noninformative priors were set for all
 525 parameters. Four independent MCMC chains were run with 1,000 and 2,000
 526 steps in the warmup and sampling iterations, respectively. We confirmed that all
 527 estimated parameters had <1.01 R-hat convergence diagnostic and >200
 528 effective sampling size values, indicating that the MCMC runs were successfully
 529 convergent. The fitted model closely recapitulated the observed viral lineage
 530 dynamics in each country (**Extended Data Fig. 2c**). The analyses above were
 531 performed in R v4.1.2 (<https://www.r-project.org/>).
 532

533 Cell culture

534 HEK293 cells (a human embryonic kidney cell line; ATCC CRL-1573) and
 535 HEK293-ACE2 cells [HEK293 cells (ATCC CRL-1573) stably expressing human
 536 ACE2]²² were maintained in DMEM (high glucose) (Sigma-Aldrich, Cat#
 537 6429-500ML) containing 10% FBS, 1 μ g/ml puromycin (InvivoGen, Cat#
 538 ant-pr-1) and 1% PS. HEK293-ACE2/TMPRSS2 cells [HEK293 cells (ATCC
 539 CRL-1573) stably expressing human ACE2 and TMPRSS2]²² were maintained
 540 in Dulbecco's modified Eagle's medium (DMEM) (high glucose) (Wako, Cat#
 541 044-29765) containing 10% foetal bovine serum (FBS) and 1%
 542 penicillin-streptomycin (PS). HEK293-C34 cells, *IFNAR1* KO HEK293 cells
 543 expressing human ACE2 and TMPRSS2 by doxycycline treatment²¹, were
 544 maintained in Dulbecco's modified Eagle's medium (high glucose)
 545 (Sigma-Aldrich, Cat# R8758-500ML) containing 10% FBS, 10 μ g/ml blasticidin

(InvivoGen, Cat# ant-bl-1) and 1% PS. Vero cells [an African green monkey (*Chlorocebus sabaeus*) kidney cell line; JCRB0111] were maintained in Eagle's minimum essential medium (EMEM) (Wako, Cat# 051-07615) containing 10% FBS and 1% PS. VeroE6/TMPRSS2 cells (VeroE6 cells stably expressing human TMPRSS2; JCRB1819)²⁹ were maintained in DMEM (low glucose) (Wako, Cat# 041-29775) containing 10% FBS, G418 (1 mg/ml; Nacalai Tesque, Cat# G8168-10ML) and 1% PS. Calu-3 cells (a human lung epithelial cell line; ATCC HTB-55) were maintained in EMEM (Sigma-Aldrich, Cat# M4655-500ML) containing 20% FBS and 1% PS. Calu-3/DSP₁₋₇ cells [Calu-3 cells (ATCC HTB-55) stably expressing DSP₁₋₇]⁴⁰ were maintained in EMEM (Wako, Cat# 056-08385) supplemented with 20% FBS and 1% PS. B16F10 cells (a mouse melanoma cell line; RCB2630) were maintained in DMEM (high glucose) (Sigma-Aldrich, Cat# D6429-500ML) containing 10% FBS and 1% PS. Expi293 cells (Thermo Fisher Scientific, Cat# A14527) were maintained in Expi293 expression medium (Thermo Fisher Scientific, Cat# A1435101). Primary human nasal epithelial cells (Cat# EP02, Batch# MP0010) were purchased from Epithelix and maintained according to the manufacturer's procedure.

Plasmid construction

Plasmids expressing the SARS-CoV-2 S proteins of B.1.1 (the parental D614G-bearing variant), Alpha (B.1.1.7), Delta (B.1.617.2) and BA.1 variants were prepared in our previous studies^{11,12,22,23,41}. Plasmids expressing the codon-optimised S proteins of BA.2 and a BA.2 derivative that loses its cytoplasmic tail were generated by site-directed overlap extension PCR using the primers listed in **Supplementary Table 3**. The resulting PCR fragment was digested with KpnI and NotI and inserted into the corresponding site of the pCAGGS vector. To construct the plasmids expressing anti-SARS-CoV-2 monoclonal antibodies (Casirivimab, Imdevimab or Sotrovimab), the sequences of the variable regions of these antibodies were obtained from KEGG Drug Database (<https://www.genome.jp/kegg/drug/>) and were artificially synthesized (Fasmac). The obtained coding sequences of the variable regions of the heavy and light chains were cloned into the pCAGGS vector containing the sequences of the human immunoglobulin 1 and kappa constant region [kindly provided by Dr. Hisashi Arase (Osaka University, Japan)]. Nucleotide sequences were determined by DNA sequencing services (Eurofins), and the sequence data were analyzed by Sequencher v5.1 software (Gene Codes Corporation).

Preparation of monoclonal antibodies

Casirivimab, Imdevimab and Sotrovimab were prepared as previously described^{11,42}. Briefly, the pCAGGS vectors containing the sequences encoding the immunoglobulin heavy and light chains were cotransfected into HEK293T

587 cells using PEI Max (Polysciences, Cat# 24765-1). At 48 h posttransfection, the
588 cell culture supernatants were harvested, and the antibodies were purified using
589 NAb protein A plus spin kit (Thermo Fisher Scientific, Cat# 89948) according to
590 the manufacturer's protocol.

591

592 **Preparation of mouse sera**

593 The SARS-CoV-2 S-immunised mouse sera were prepared as previously
594 described⁴². To prepare the immunogen, B16F10 cells (2,500,000 cells) were
595 transfected with 5 µg S expression plasmid by PEI Max (Polysciences, Cat#
596 24765-1) according to the manufacturer's protocol. Two days posttransfection,
597 the transfected cells were washed twice with PBS, and then the cell pellets were
598 stored at -80°C (10,000,000 cells per stock). The expression of transfected S
599 protein was verified by flow cytometry and western blot. BALB/c mice (female, 7
600 weeks old) were purchased from Japan SLC Inc. (Shizuoka, Japan). The mice
601 were maintained under specific pathogen-free conditions. For the immunisation,
602 mice were subcutaneously immunized with the freeze-thawed S-expressing
603 B16F10 cells in complete Freund's adjuvant (50%) (Sigma-Aldrich, Cat# F5881).
604 Three weeks after immunisation, blood was collected in BD Microtainer blood
605 collection tubes (BD Biosciences, Cat# 365967) and sera were collected by
606 centrifugation.

607

608 **Neutralisation assay**

609 Pseudoviruses were prepared as previously described^{11,23,24,41,43}. Briefly,
610 lentivirus (HIV-1)-based, luciferase-expressing reporter viruses were
611 pseudotyped with the SARS-CoV-2 spikes. HEK293T cells (1,000,000 cells)
612 were cotransfected with 1 µg psPAX2-IN/HiBiT⁴⁴, 1 µg pWPI-Luc2⁴⁴, and 500 ng
613 plasmids expressing parental S or its derivatives using PEI Max (Polysciences,
614 Cat# 24765-1) according to the manufacturer's protocol. Two days
615 posttransfection, the culture supernatants were harvested and centrifuged. The
616 pseudoviruses were stored at -80°C until use.

617 For the neutralisation assay, the SARS-CoV-2 S pseudoviruses
618 (counting ~20,000 relative light units) were incubated with serially diluted
619 (40-fold to 29,160-fold dilution at the final concentration) heat-inactivated sera or
620 monoclonal antibodies (Casirivimab, Imdevimab or Sotrovimab) at 37°C for 1 h.
621 Pseudoviruses without sera were included as controls. Then, an 80 µl mixture of
622 pseudovirus and serum/antibody was added to HOS-ACE2/TMPRSS2 cells
623 (10,000 cells/50 µl) in a 96-well white plate. At 2 d.p.i., the infected cells were
624 lysed with a One-Glo luciferase assay system (Promega, Cat# E6130) or a
625 Bright-GloTM Luciferase Assay System (Promega, Cat# E2650), and the
626 luminescent signal was measured using a GloMax explorer multimode

microplate reader 3500 (Promega) or CentroXS3 (Berthold Technologies). The assay of each serum was performed in triplicate, and the 50% neutralisation titre (NT50) was calculated using Prism 9 (GraphPad Software).

SARS-CoV-2 reverse genetics

Recombinant SARS-CoV-2 was generated by circular polymerase extension reaction (CPER) as previously described²¹⁻²³. In brief, 9 DNA fragments encoding the partial genome of SARS-CoV-2 (strain WK-521, PANGO lineage A; GISAID ID: EPI_ISL_408667)²⁹ were prepared by PCR using PrimeSTAR GXL DNA polymerase (Takara, Cat# R050A). A linker fragment encoding hepatitis delta virus ribozyme, bovine growth hormone poly A signal and cytomegalovirus promoter was also prepared by PCR. The corresponding SARS-CoV-2 genomic region and the PCR templates and primers used for this procedure are summarised in **Supplementary Table 4**. The 10 obtained DNA fragments were mixed and used for CPER²¹. To prepare GFP-expressing replication-competent recombinant SARS-CoV-2, we used fragment 9, in which the *GFP* gene was inserted in the *ORF7a* frame, instead of the authentic F9 fragment (see **Extended Data Fig. 4** and **Supplementary Table 4**)²¹.

To produce recombinant SARS-CoV-2, the CPER products were transfected into HEK293-C34 cells using TransIT-LT1 (Takara, Cat# MIR2300) according to the manufacturer's protocol. At one day posttransfection, the culture medium was replaced with Dulbecco's modified Eagle's medium (high glucose) (Sigma-Aldrich, Cat# R8758-500ML) containing 2% FCS, 1% PS and doxycycline (1 µg/ml; Takara, Cat# 1311N). At six days posttransfection, the culture medium was harvested and centrifuged, and the supernatants were collected as the seed virus. To remove the CPER products (i.e., SARS-CoV-2-related DNA), 1 ml of the seed virus was treated with 2 µl TURBO DNase (Thermo Fisher Scientific, Cat# AM2238) and incubated at 37°C for 1 h. Complete removal of the CPER products (i.e., SARS-CoV-2-related DNA) from the seed virus was verified by PCR. The working virus stock was prepared from the seed virus as described above.

To generate chimeric recombinant SARS-CoV-2 that encodes the S proteins of B.1.1, BA.1 and BA.2 (**Extended Data Fig. 4**), mutations were inserted in fragment 8 (**Supplementary Table 4**) using the GENEART site-directed mutagenesis system (Thermo Fisher Scientific, Cat# A13312) according to the manufacturer's protocol with the primers listed in **Supplementary Table 5**. A recombinant SARS-CoV-2 that bears D614G S (corresponds to B.1.1 S) was prepared in our previous study²³. To prepare a chimeric recombinant SARS-CoV-2 that bears Delta S (**Extended Data Fig. 4**), the fragment of viral genome that corresponds to the region of fragment 8 (**Supplementary Table 4**) was subcloned from a Delta isolate (strain

668 TKYTK1734; GISAID ID: EPI_ISL_2378732)²³. Nucleotide sequences were
669 determined by a DNA sequencing service (Fasmac), and the sequence data
670 were analysed by Sequencher software v5.1 (Gene Codes Corporation).

671 To produce chimeric recombinant SARS-CoV-2, the CPER products
672 were transfected into HEK293-C34 cells using TransIT-LT1 (Takara, Cat#
673 MIR2300) according to the manufacturer's protocol. At 1 day posttransfection,
674 the culture medium was replaced with Dulbecco's modified Eagle's medium
675 (high glucose) (Sigma-Aldrich, Cat# R8758-500ML) containing 2% FCS, 1% PS
676 and doxycycline (1 µg/ml; Takara, Cat# 1311N). At 7 days posttransfection, the
677 culture medium was harvested and centrifuged, and the supernatants were
678 collected as the seed virus. To remove the CPER products (i.e.,
679 SARS-CoV-2-related DNA), 1 ml of the seed virus was treated with 2 µl TURBO
680 DNase (Thermo Fisher Scientific, Cat# AM2238) and incubated at 37°C for 1 h.
681 Complete removal of the CPER products (i.e., SARS-CoV-2-related DNA) from
682 the seed virus was verified by PCR. The working virus stock was prepared from
683 the seed virus as described below (see "SARS-CoV-2 preparation and titration"
684 section).

685

686 **SARS-CoV-2 preparation and titration**

687 The working virus stocks of chimeric recombinant SARS-CoV-2 that encodes the
688 S proteins of B.1.1, Delta, BA.1 and BA.2 were prepared and titrated as
689 previously described²¹⁻²³. In brief, 20 µl of the seed virus was inoculated into
690 VeroE6/TMPRSS2 cells (5,000,000 cells in a T-75 flask). One hour after
691 infection (h.p.i.), the culture medium was replaced with DMEM (low glucose)
692 (Wako, Cat# 041-29775) containing 2% FBS and 1% PS. At 3 d.p.i., the culture
693 medium was harvested and centrifuged, and the supernatants were collected as
694 the working virus stock.

695 The titre of the prepared working virus was measured as the 50%
696 tissue culture infectious dose (TCID₅₀). Briefly, one day before infection,
697 VeroE6/TMPRSS2 cells (10,000 cells) were seeded into a 96-well plate. Serially
698 diluted virus stocks were inoculated into the cells and incubated at 37°C for 4 d.
699 The cells were observed under microscopy to judge the CPE appearance. The
700 value of TCID₅₀/ml was calculated with the Reed–Muench method⁴⁵.

701 To verify the sequence of chimeric recombinant SARS-CoV-2, viral
702 RNA was extracted from the working viruses using a QIAamp viral RNA mini kit
703 (Qiagen, Cat# 52906) and viral genome sequence was analysed as described
704 above (see "Viral genome sequencing" section). In brief, the viral sequences of
705 GFP-encoding recombinant SARS-CoV-2 (strain WK-521; GISAID ID:
706 EPI_ISL_408667)^{21,29} that harbour the S genes of respective variants (B.1.1,
707 BA.1 or BA.2) were used for the reference. Information on the unexpected

708 mutations detected is summarized in **Supplementary Table 6**, and the raw data
709 are deposited in Gene Expression Omnibus (accession number: GSE196649).

710

711 **SARS-CoV-2 infection**

712 One day before infection, Vero cells (10,000 cells), VeroE6/TMPRSS2 cells
713 (10,000 cells), Calu-3 cells (20,000 cells), HEK293-ACE2 cells (10,000 cells),
714 HEK293-ACE2/TMPRSS2 cells (10,000 cells), were seeded into a 96-well plate.
715 SARS-CoV-2 [100 TCID₅₀ for VeroE6/TMPRSS2 cells (**Fig. 3a**), 1,000 TCID₅₀
716 for Vero cells (**Fig. 3a**), HEK293-ACE2 cells (10,000 cells) (**Fig. 3j**), and
717 HEK293-ACE2/TMPRSS2 cells (10,000 cells) (**Fig. 3j**); and 2,000 TCID₅₀ for
718 Calu-3 cells (**Fig. 3a**)] was inoculated and incubated at 37°C for 1 h. The
719 infected cells were washed, and 180 µl of culture medium was added. The
720 culture supernatant (10 µl) was harvested at the indicated timepoints and used
721 for RT-qPCR to quantify the viral RNA copy number (see “RT-qPCR” section
722 below).

723 The infection experiment primary human nasal epithelial cells (**Fig. 3a**)
724 was performed as previously described^{11,23}. Briefly, the working viruses were
725 diluted with Opti-MEM (Thermo Fisher Scientific, Cat# 11058021). The diluted
726 viruses (1,000 TCID₅₀ in 100 µl) were inoculated onto the apical side of the
727 culture and incubated at 37°C for 1 h. The inoculated viruses were removed and
728 washed twice with Opti-MEM. To harvest the viruses on the apical side of the
729 culture, 100 µl Opti-MEM was applied onto the apical side of the culture and
730 incubated at 37°C for 10 m. The Opti-MEM applied was harvested and used for
731 RT-qPCR to quantify the viral RNA copy number (see “RT-qPCR” section
732 below).

733

734 **RT-qPCR**

735 RT-qPCR was performed as previously described^{11,12,22,23}. Briefly, 5 µl of culture
736 supernatant was mixed with 5 µl of 2 × RNA lysis buffer [2% Triton X-100, 50
737 mM KCl, 100 mM Tris-HCl (pH 7.4), 40% glycerol, 0.8 U/µl recombinant RNase
738 inhibitor (Takara, Cat# 2313B)] and incubated at room temperature for 10 min.
739 RNase-free water (90 µl) was added, and the diluted sample (2.5 µl) was used
740 as the template for real-time RT-PCR performed according to the manufacturer’s
741 protocol using the One Step TB Green PrimeScript PLUS RT-PCR kit (Takara,
742 Cat# RR096A) and the following primers: Forward *N*, 5'-AGC CTC TTC TCG
743 TTC CTC ATC AC-3'; and Reverse *N*, 5'-CCG CCA TTG CCA GCC ATT C-3'.
744 The viral RNA copy number was standardized with a SARS-CoV-2 direct
745 detection RT-qPCR kit (Takara, Cat# RC300A). Fluorescent signals were
746 acquired using QuantStudio 3 Real-Time PCR system (Thermo Fisher Scientific),
747 CFX Connect Real-Time PCR Detection system (Bio-Rad), Eco Real-Time PCR

748 System (Illumina), qTOWER3 G Real-Time System (Analytik Jena) or 7500
749 Real-Time PCR System (Thermo Fisher Scientific).

750

751 **Fluorescence microscopy**

752 Fluorescence microscopy (**Fig. 3b** and **Extended Data Fig. 5a**) was performed
753 as previously described²³. Briefly, one day before infection, VeroE6/TMPRSS2
754 cells (10,000 cells) were seeded into 96-well, glass bottom, black plates and
755 infected with SARS-CoV-2 (100 TCID₅₀). At 24, 48, and 72 h.p.i., GFP
756 fluorescence was observed under an All-in-One Fluorescence Microscope
757 BZ-X800 (Keyence) in living cells, and a 13-square-millimeter area of each
758 sample was scanned. Images were reconstructed using an BZ-X800 analyzer
759 software (Keyence), and the area of the GFP-positive cells was measured using
760 this software.

761

762 **Plaque assay**

763 Plaque assay (**Fig. 3c** and **Extended Data Fig. 5b**) was performed as
764 previously described^{12,22,23}. Briefly, one day before infection, VeroE6/TMPRSS2
765 cells (100,000 cells) were seeded into a 24-well plate and infected with
766 SARS-CoV-2 (1, 10, 100 and 1,000 TCID₅₀) at 37°C for 2 h. Mounting solution
767 containing 3% FBS and 1.5% carboxymethyl cellulose (Wako, Cat# 039-01335)
768 was overlaid, followed by incubation at 37°C. At 3 d.p.i., the culture medium was
769 removed, and the cells were washed with PBS three times and fixed with 4%
770 paraformaldehyde phosphate (Nacalai Tesque, Cat# 09154-85). The fixed cells
771 were washed with tap water, dried, and stained with staining solution [0.1%
772 methylene blue (Nacalai Tesque, Cat# 22412-14) in water] for 30 m. The stained
773 cells were washed with tap water and dried, and the size of plaques was
774 measured using Fiji software v2.2.0 (ImageJ).

775

776 **Coculture experiment**

777 Coculture experiment (**Extended Data Fig. 5c**) was performed as previously
778 described¹². Briefly, one day before transfection, effector cells (i.e., S-expressing
779 cells) were seeded on the poly-L-lysine (Sigma, Cat# P4832) coated coverslips
780 put in a 12-well plate, and target cells were prepared at a density of 100,000
781 cells in a 12-well plate. To prepare effector cells, HEK293 cells were
782 cotransfected with the S-expression plasmids (500 ng) and pDSP₈₋₁₁ (500 ng)
783 using PEI Max (Polysciences, Cat# 24765-1). To prepare target cells, HEK293
784 and HEK293-ACE2/TMPRSS2 cells were transfected with pDSP₁₋₇ (500 ng). At
785 24 h posttransfection, target cells were detached and cocultured with effector
786 cells in a 1:2 ratio. At 9 h post-coculture, cells were fixed with 4%
787 paraformaldehyde in PBS (Nacalai Tesque, Cat# 09154-85) for 15 m at room
788 temperature. Nuclei were stained with Hoechst 33342 (Thermo Fisher Scientific,

789 Cat# H3570). The coverslips were mounted on glass slides using
790 Fluoromount-G (Southern Biotechnology, Cat# 0100-01) with Hoechst 33342
791 and observed using an A1Rsi Confocal Microscope (Nikon). The size of
792 syncytium (GFP-positive area) was measured using Fiji software v2.2.0
793 (ImageJ) as previously described¹².

794

SARS-CoV-2 S-based fusion assay

796 SARS-CoV-2 S-based fusion assay (**Fig. 3d and 3f**) was performed as
797 previously described^{12,22,23}. This assay utilizes a dual split protein (DSP)
798 encoding *Renilla* luciferase and *GFP* genes; the respective split proteins,
799 DSP₈₋₁₁ and DSP₁₋₇, are expressed in effector and target cells by transfection.
800 Briefly, on day 1, effector cells (i.e., S-expressing cells) and target cells (see
801 below) were prepared at a density of 0.6–0.8 × 10⁶ cells in a 6-well plate. To
802 prepare effector cells, HEK293 cells were cotransfected with the S expression
803 plasmids (400 ng) and pDSP₈₋₁₁ (400 ng) using TransIT-LT1 (Takara, Cat#
804 MIR2300). To prepare target cells, HEK293 cells were cotransfected with
805 pC-ACE2 (200 ng) and pDSP₁₋₇ (400 ng). Target HEK293 cells in selected wells
806 were cotransfected with pC-TMPRSS2 (40 ng) in addition to the plasmids above.
807 VeroE6/TMPRSS2 cells, Calu-3 cells, HEK293-ACE2 cells and
808 HEK293-ACE2/TMPRSS2 cells were transfected with pDSP₁₋₇ (400ng). On day
809 3 (24 h posttransfection), 16,000 effector cells were detached and reseeded into
810 96-well black plates (PerkinElmer, Cat# 6005225), and target cells (HEK293,
811 VeroE6/TMPRSS2 or Calu-3/DSP₁₋₇ cells) were reseeded at a density of
812 1,000,000 cells/2 ml/well in 6-well plates. On day 4 (48 h posttransfection), target
813 cells were incubated with EnduRen live cell substrate (Promega, Cat# E6481)
814 for 3 h and then detached, and 32,000 target cells were added to a 96-well plate
815 with effector cells. *Renilla* luciferase activity was measured at the indicated time
816 points using Centro XS3 LB960 (Berthold Technologies). To measure the
817 surface expression level of S protein, effector cells were stained with rabbit
818 anti-SARS-CoV-2 S S1/S2 polyclonal antibody (Thermo Fisher Scientific, Cat#
819 PA5-112048, 1:100). Normal rabbit IgG (SouthernBiotech, Cat# 0111-01, 1:100)
820 was used as negative controls, and APC-conjugated goat anti-rabbit IgG
821 polyclonal antibody (Jackson ImmunoResearch, Cat# 111-136-144, 1:50) was
822 used as a secondary antibody. Surface expression level of S proteins
823 (**Extended Data Fig. 6a**) was measured using FACS Canto II (BD Biosciences)
824 and the data were analysed using FlowJo software v10.7.1 (BD Biosciences).
825 Gating strategy for flow cytometry is shown in **Supplementary Fig. 1**. To
826 calculate fusion activity, *Renilla* luciferase activity was normalized to the MFI of
827 surface S proteins. The normalized value (i.e., *Renilla* luciferase activity per the
828 surface S MFI) is shown as fusion activity.

829

830 Yeast surface display

831 Yeast surface display (**Extended Data Fig. 6b**) was performed as previously
832 described as previously described^{22,24,46}. Briefly, the peptidase domain of human
833 ACE2 (residues 18-740) was expressed in Expi293 cells and purified by a 5-ml
834 HisTrap Fast Flow column (Cytiva, Cat# 17-5255-01) and Superdex 200 16/600
835 (Cytiva, Cat# 28-9893-35) using an ÄKTA pure chromatography system (Cytiva),
836 and the purified soluble ACE2 was labelled with CF640 (Biotium, Cat# 92108).
837 Protein quality was verified using a Tycho NT.6 system (NanoTemper) and
838 ACE2 activity assay kit (Sensolyte, Cat# AS-72086).

839 An enhanced yeast display platform for SARS-CoV-2 RBD [wild-type
840 (B.1.1), residues 336-528] yeast surface expression was established using
841 *Saccharomyces cerevisiae* EBY100 strain and pJYDC1 plasmid (Addgene, Cat#
842 162458) as previously described^{22,24,47}. The yeast-optimized
843 SARS-CoV-2_RBD-Omicron-BA.1 gene (**Supplementary Table 7**) was
844 obtained from Twist Biosciences. The site-directed mutagenesis was performed
845 using the KAPA HiFi HotStart ReadyMix kit (Roche, Cat# KK2601) by restriction
846 enzyme-free cloning procedure⁴⁸. Primers for mutagenesis are listed in
847 **Supplementary Table 8**.

848 The binding affinity of SARS-CoV-2 S B.1.1, BA.1, and BA.2 RBDs to
849 human ACE2 were titrated by flow cytometry. The CF640-labelled ACE2 at
850 12–14 different concentrations (200 nM to 13 pM in PBS supplemented with
851 bovine serum albumin at 1 g/l) per measurement were incubated with expressed
852 yeast aliquots and 1 nM bilirubin (Sigma-Aldrich, Cat# 14370-1G) and analysed
853 by using FACS S3e Cell Sorter device (Bio-Rad) as previously described^{22,24,47}.
854 The background binding subtracted fluorescent signal was fitted to a standard
855 noncooperative Hill equation by nonlinear least-squares regression using Python
856 v3.7 (<https://www.python.org>) as previously described⁴⁷.

858 TMPRSS2 expression on the cell surface

859 To measure the surface expression level of TMPRSS2 (**Extended Data Fig. 6c**),
860 HEK293-ACE2 cells and HEK293-ACE2/TMPRSS2 cells were stained with
861 rabbit anti-TMPRSS2 polyclonal antibody (BIOSS, Cat# BS-6285R, 1:100).
862 Normal rabbit IgG (SouthernBiotech, Cat# 0111-01, 1:100) was used as
863 negative controls, and APC-conjugated goat anti-rabbit IgG polyclonal antibody
864 (Jackson ImmunoResearch, Cat# 111-136-144, 1:50) was used as a secondary
865 antibody. Surface expression level of TMPRSS2 was measured using FACS
866 Canto II (BD Biosciences) and the data were analysed using FlowJo software
867 v10.7.1 (BD Biosciences). Gating strategy for flow cytometry is shown in
868 **Supplementary Fig. 1**.

870 Western blot

Western blot (**Fig. 3e**) was performed as previously described^{12,22,23}. The HEK293 cells cotransfected with the S expression plasmids and pDSP₈₋₁₁ (see “SARS-CoV-2 S-based fusion assay” section above) were used. To quantify the level of the cleaved S2 protein in the cells, the harvested cells were washed and lysed in lysis buffer [25 mM HEPES (pH 7.2), 20% glycerol, 125 mM NaCl, 1% Nonidet P40 substitute (Nacalai Tesque, Cat# 18558-54), protease inhibitor cocktail (Nacalai Tesque, Cat# 03969-21)]. After quantification of total protein by protein assay dye (Bio-Rad, Cat# 5000006), lysates were diluted with 2 × sample buffer [100 mM Tris-HCl (pH 6.8), 4% SDS, 12% β-mercaptoethanol, 20% glycerol, 0.05% bromophenol blue] and boiled for 10 m. Then, 10 μl samples (50 μg of total protein) were subjected to Western blot. For protein detection, the following antibodies were used: mouse anti-SARS-CoV-2 S monoclonal antibody (clone 1A9, GeneTex, Cat# GTX632604, 1:10,000), rabbit anti-beta actin (ACTB) monoclonal antibody (clone 13E5, Cell Signalling, Cat# 4970, 1:5,000), horseradish peroxidase (HRP)-conjugated donkey anti-rabbit IgG polyclonal antibody (Jackson ImmunoResearch, Cat# 711-035-152, 1:10,000) and HRP-conjugated donkey anti-mouse IgG polyclonal antibody (Jackson ImmunoResearch, Cat# 715-035-150, 1:10,000). Chemiluminescence was detected using SuperSignal West Femto Maximum Sensitivity Substrate (Thermo Fisher Scientific, Cat# 34095) according to the manufacturer’s instruction. Bands were visualized using an Amersham Imager 600 (GE Healthcare), and the band intensity was quantified using Image Studio Lite v5.2 (LI-COR Biosciences) or Fiji software v2.2.0 (ImageJ). Uncropped blots are shown in **Supplementary Fig. 2**.

Pseudovirus infection

Pseudovirus infection was (**Fig. 3g**) performed as previously described^{11,12,22-24,43}. Briefly, the same amount of pseudoviruses (normalized to the HiBiT value, which indicates the amount of p24 HIV-1 antigen) was inoculated into HEK293-ACE2 cells or HEK293-ACE2/TMPRSS2 and viral infectivity was measured as described above (see “Neutralisation assay” section). To analyse the effect of TMPRSS2 for pseudovirus infectivity, the fold change of the values of HEK293-ACE2/TMPRSS2 to HEK293-ACE2 was calculated.

Animal experiments

Animal experiments (**Fig. 4**) were performed as previously described^{12,23}. Syrian hamsters (male, 4 weeks old) were purchased from Japan SLC Inc. (Shizuoka, Japan). Baseline body weights were measured before infection. For the virus infection experiments, hamsters were euthanized by intramuscular injection of a mixture of either 0.15 mg/kg medetomidine hydrochloride (Domitor®, Nippon

Zenyaku Kogyo), 2.0 mg/kg midazolam (Dormicum[®], FUJIFILM Wako Chemicals) and 2.5 mg/kg butorphanol (Vetorphale[®], Meiji Seika Pharma), or 0.15 mg/kg medetomidine hydrochloride, 2.0 mg/kg alphaxalone (Alfaxan[®], Jurox) and 2.5 mg/kg butorphanol. The B.1.1 virus, Delta, Omicron (10,000 TCID₅₀ in 100 µl), or saline (100 µl) were intranasally inoculated under anaesthesia. Oral swabs were daily collected under anaesthesia with isoflurane (Sumitomo Dainippon Pharma). Body weight, enhanced pause (Penh), the ratio of time to peak expiratory flow relative to the total expiratory time (Rpef) and subcutaneous oxygen saturation (SpO₂) were routinely monitored at indicated timepoints (see “Lung function test” section below). Respiratory organs were anatomically collected at 1, 3 and 5 d.p.i (for lung) or 1 d.p.i. (for trachea). Viral RNA load in the respiratory tissues were determined by RT-qPCR. The respiratory tissues were also used for histopathological and IHC analyses (see “H&E staining” and “IHC” sections below).

Lung function test

Lung function test (**Fig. 4a**) was performed as previously described¹². Respiratory parameters (Penh and Rpef) were measured by using a whole-body plethysmography system (DSI) according to the manufacturer's instructions. In brief, a hamster was placed in an unrestrained plethysmography chamber and allowed to acclimatize for 30 s, then, data were acquired over a 4-m period by using FinePointe Station and Review softwares v2.9.2.12849 (STARR). The state of oxygenation was examined by measuring SpO₂ using pulse oximeter, MouseOx PLUS (STARR). SpO₂ was measured by attaching a measuring chip to the neck of hamsters sedated by 0.25 mg/kg medetomidine hydrochloride.

IHC

IHC (**Extended Data Fig. 7**) was performed as previously described^{12,23} using an Autostainer Link 48 (Dako). The deparaffinized sections were exposed to EnVision FLEX target retrieval solution high pH (Agilent, Cat# K8004) for 20 m at 97°C to activate, and mouse anti-SARS-CoV-2 N monoclonal antibody (R&D systems, Clone 1035111, Cat# MAB10474-SP, 1:400) was used as a primary antibody. The sections were sensitized using EnVision FLEX (Agilent) for 15 m and visualised by peroxidase-based enzymatic reaction with 3,3'-diaminobenzidine tetrahydrochloride as substrate for 5 m. The N protein positivity (**Fig. 4c and 4d**) was evaluated by certificated pathologists as previously described¹². Images were incorporated as virtual slide by NDRscan3.2 software (Hamamatsu Photonics). The N-protein positivity was measured as the area using Fiji software v2.2.0 (ImageJ).

H&E staining

H&E staining (**Extended Data Fig. 8**) was performed as previously described^{12,23}. Briefly, excised animal tissues were fixed with 10% formalin neutral buffer solution, and processed for paraffin embedding. The paraffin blocks were sectioned with 3 µm-thickness and then mounted on silane-coated glass slides (MAS-GP, Matsunami). H&E staining was performed according to a standard protocol.

Histopathological scoring

Histopathological scoring (**Fig. 4e** and **Extended Data Fig. 8a**) was performed as previously described^{12,23}. Pathological features including bronchitis or bronchiolitis, haemorrhage with congestive edema, alveolar damage with epithelial apoptosis and macrophage infiltration, hyperplasia of type II pneumocytes, and the area of the hyperplasia of large type II pneumocytes were evaluated by certified pathologists and the degree of these pathological findings were arbitrarily scored using four-tiered system as 0 (negative), 1 (weak), 2 (moderate), and 3 (severe). The "large type II pneumocytes" are the hyperplasia of type II pneumocytes exhibiting more than 10-µm-diameter nucleus. We described "large type II pneumocytes" as one of the remarkable histopathological features reacting SARS-CoV-2 infection in our previous studies^{12,23}. Total histology score is the sum of these five indices.

To measure the inflammation area in the infected lungs (**Extended Data Fig. 8b**), four hamsters infected with each virus were sacrificed at the 1, 3 and 5 d.p.i., and all four right lung lobes, including upper (anterior/cranial), middle, lower (posterior/caudal), and accessory lobes, were sectioned along with their bronchi. The tissue sections were stained by H&E, and the digital microscopic images were incorporated into virtual slides using NDRscan3.2 software (Hamamatsu Photonics). The inflammatory area including type II pneumocyte hyperplasia in the infected whole lungs was morphometrically analysed using Fiji software v2.2.0 (ImageJ).

Statistics and reproducibility

Statistical significance was tested using a two-sided Student's *t*-test or a two-sided Mann–Whitney *U*-test unless otherwise noted. The tests above were performed using Prism 9 software v9.1.1 (GraphPad Software).

In the time-course experiments (**Fig. 3a, 3d, 3f, 3h, 4a–4c, and 4e**), a multiple regression analysis including experimental conditions (i.e., the types of infected viruses) as explanatory variables and timepoints as qualitative control variables was performed to evaluate the difference between experimental conditions thorough all timepoints. *P* value was calculated by a two-sided Wald test. Subsequently, familywise error rates (FWERs) were calculated by the Holm method. These analyses were performed in v4.1.2 (<https://www.r-project.org/>).

In **Extended Data Fig. 7 and 8**, photographs shown are the representative areas of at least two independent experiments by using four hamsters at each timepoint. In **Extended Data Fig. 5**, assays were performed in triplicate. Photographs shown are the representatives of >20 fields of view taken for each sample.

999

1000 **Data availability**

1001 The raw data of virus sequences analysed in this study are deposited in Gene
1002 Expression Omnibus (accession number: GSE196649). All databases/datasets
1003 used in this study are available from GISAID database (<https://www.gisaid.org>)
1004 and Genbank database (<https://www.ncbi.nlm.nih.gov/genbank/>). The accession
1005 numbers of viral sequences used in this study are listed in Method section.

1006

1007 **Code availability**

1008 The computational code to estimate the relative effective reproduction number of
1009 each viral lineage (**Fig. 1**) is available in the GitHub repository
1010 ([https://github.com/TheSatoLab/Omicron_BA2/tree/main/lineage_growth_hierar](https://github.com/TheSatoLab/Omicron_BA2/tree/main/lineage_growth_hierarchical_model)
1011 [chical_model](https://github.com/TheSatoLab/Omicron_BA2/tree/main/lineage_growth_hierarchical_model)).

1012 References

- 1013 1 WHO. "Classification of Omicron (B.1.1.529): SARS-CoV-2 variant of
1014 concern (November 26, 2021)"
1015 [https://www.who.int/news/item/26-11-2021-classification-of-omicron-\(b.1.
1016 1.529\)-sars-cov-2-variant-of-concern](https://www.who.int/news/item/26-11-2021-classification-of-omicron-(b.1.1.529)-sars-cov-2-variant-of-concern). (2021).
- 1017 2 WHO. "Tracking SARS-CoV-2 variants (February 3, 2022)".
1018 <https://www.who.int/en/activities/tracking-SARS-CoV-2-variants/>.
1019 (2022).
- 1020 3 UKHSA. "SARS-CoV-2 variants of concern and variants under
1021 investigation in England. Technical briefing 35 (January 28, 2022)".
1022 [https://assets.publishing.service.gov.uk/government/uploads/system/uplo
1023 ads/attachment_data/file/1050999/Technical-Briefing-35-28January2022.
1024 pdf](https://assets.publishing.service.gov.uk/government/uploads/system/uploads/attachment_data/file/1050999/Technical-Briefing-35-28January2022.pdf). (2022).
- 1025 4 Cele, S. *et al.* Omicron extensively but incompletely escapes Pfizer
1026 BNT162b2 neutralization. *Nature*, doi:
1027 <https://doi.org/10.1038/d41586-41021-03824-41585> (2021).
- 1028 5 Cao, Y. *et al.* Omicron escapes the majority of existing SARS-CoV-2
1029 neutralizing antibodies. *Nature*, doi:
1030 <https://doi.org/10.1038/d41586-41021-03796-41586> (2021).
- 1031 6 Dejnirattisai, W. *et al.* Reduced neutralisation of SARS-CoV-2 omicron
1032 B.1.1.529 variant by post-immunisation serum. *Lancet*,
1033 doi:[https://doi.org/10.1016/S0140-6736\(1021\)02844-02840](https://doi.org/10.1016/S0140-6736(1021)02844-02840) (2021).
- 1034 7 Cameroni, E. *et al.* Broadly neutralizing antibodies overcome
1035 SARS-CoV-2 Omicron antigenic shift. *Nature*, doi:
1036 <https://doi.org/10.1038/d41586-41021-03825-41584> (2021).
- 1037 8 Garcia-Beltran, W. F. *et al.* mRNA-based COVID-19 vaccine boosters
1038 induce neutralizing immunity against SARS-CoV-2 Omicron variant. *Cell*,
1039 doi: <https://doi.org/10.1016/j.cell.2021.1012.1033> (2021).
- 1040 9 Planas, D. *et al.* Considerable escape of SARS-CoV-2 Omicron to
1041 antibody neutralization. *Nature*, doi:
1042 <https://doi.org/10.1038/d41586-41021-03827-41582> (2021).
- 1043 10 Liu, L. *et al.* Striking antibody evasion manifested by the Omicron variant
1044 of SARS-CoV-2. *Nature*, doi:
1045 <https://doi.org/10.1038/d41586-41021-03826-41583> (2021).
- 1046 11 Meng, B. *et al.* Altered TMPRSS2 usage by SARS-CoV-2 Omicron
1047 impacts tropism and fusogenicity. *Nature*,
1048 doi:10.1038/s41586-022-04474-x (2022).
- 1049 12 Suzuki, R. *et al.* Attenuated fusogenicity and pathogenicity of
1050 SARS-CoV-2 Omicron variant. *Nature*, doi:10.1038/s41586-022-04462-1
1051 (2022).
- 1052 13 Shuai, H. *et al.* Attenuated replication and pathogenicity of SARS-CoV-2

- 1053 B.1.1.529 Omicron. *Nature*, doi:10.1038/s41586-022-04442-5 (2022).
- 1054 14 Halfmann, P. J. *et al.* SARS-CoV-2 Omicron virus causes attenuated
1055 disease in mice and hamsters. *Nature*, doi:10.1038/s41586-022-04441-6
1056 (2022).
- 1057 15 Han, P. *et al.* Receptor binding and complex structures of human ACE2 to
1058 spike RBD from omicron and delta SARS-CoV-2. *Cell*,
1059 doi:10.1016/j.cell.2022.01.001 (2022).
- 1060 16 Dejnirattisai, W. *et al.* SARS-CoV-2 Omicron-B.1.1.529 leads to
1061 widespread escape from neutralizing antibody responses. *Cell* **185**,
1062 467-484 e415, doi:10.1016/j.cell.2021.12.046 (2022).
- 1063 17 Cameroni, E. *et al.* Broadly neutralizing antibodies overcome
1064 SARS-CoV-2 Omicron antigenic shift. *Nature*,
1065 doi:10.1038/s41586-021-04386-2 (2021).
- 1066 18 Takashita, E. *et al.* Efficacy of Antibodies and Antiviral Drugs against
1067 Covid-19 Omicron Variant. *N Engl J Med*, doi:10.1056/NEJMc2119407
1068 (2022).
- 1069 19 VanBlargan, L. A. *et al.* An infectious SARS-CoV-2 B.1.1.529 Omicron
1070 virus escapes neutralization by therapeutic monoclonal antibodies. *Nat*
1071 *Med*, doi:10.1038/s41591-021-01678-y (2022).
- 1072 20 Viana, R. *et al.* Rapid epidemic expansion of the SARS-CoV-2 Omicron
1073 variant in southern Africa. *Nature*, doi:10.1038/s41586-022-04411-y
1074 (2022).
- 1075 21 Torii, S. *et al.* Establishment of a reverse genetics system for
1076 SARS-CoV-2 using circular polymerase extension reaction. *Cell Rep* **35**,
1077 109014 (2021).
- 1078 22 Motozono, C. *et al.* SARS-CoV-2 spike L452R variant evades cellular
1079 immunity and increases infectivity. *Cell Host Microbe* **29**, 1124-1136,
1080 doi:10.1016/j.chom.2021.06.006 (2021).
- 1081 23 Saito, A. *et al.* Enhanced fusogenicity and pathogenicity of SARS-CoV-2
1082 Delta P681R mutation. *Nature*, doi:10.1038/s41586-021-04266-9 (2021).
- 1083 24 Kimura, I. *et al.* The SARS-CoV-2 Lambda variant exhibits enhanced
1084 infectivity and immune resistance. *Cell Rep*, doi:
1085 <https://doi.org/10.1016/j.celrep.2021.110218> (2021).
- 1086 25 Schubert, M. *et al.* Human serum from SARS-CoV-2 vaccinated and
1087 COVID-19 patients shows reduced binding to the RBD of SARS-CoV-2
1088 Omicron variant. *MedRxiv*, doi:
1089 <https://doi.org/10.1101/2021.1112.1110.21267523> (2022).
- 1090 26 Wu, L. *et al.* SARS-CoV-2 Omicron RBD shows weaker binding affinity
1091 than the currently dominant Delta variant to human ACE2. *Signal*
1092 *Transduct Target Ther* **7**, 8, doi:10.1038/s41392-021-00863-2 (2022).
- 1093 27 Mlcochova, P. *et al.* SARS-CoV-2 B.1.617.2 Delta variant replication and

1094 immune evasion. *Nature* **599**, 114-119, doi:10.1038/s41586-021-03944-y
1095 (2021).
1096 28 Chen, S., Zhou, Y., Chen, Y. & Gu, J. fastp: an ultra-fast all-in-one
1097 FASTQ preprocessor. *Bioinformatics* **34**, i884-i890,
1098 doi:10.1093/bioinformatics/bty560 (2018).
1099 29 Matsuyama, S. *et al.* Enhanced isolation of SARS-CoV-2 by
1100 TMPRSS2-expressing cells. *Proc Natl Acad Sci U S A* **117**, 7001-7003,
1101 doi:10.1073/pnas.2002589117 (2020).
1102 30 Li, H. & Durbin, R. Fast and accurate short read alignment with
1103 Burrows-Wheeler transform. *Bioinformatics* **25**, 1754-1760,
1104 doi:10.1093/bioinformatics/btp324 (2009).
1105 31 Li, H. *et al.* The Sequence Alignment/Map format and SAMtools.
1106 *Bioinformatics* **25**, 2078-2079, doi:10.1093/bioinformatics/btp352 (2009).
1107 32 Cingolani, P. *et al.* A program for annotating and predicting the effects of
1108 single nucleotide polymorphisms, SnpEff: SNPs in the genome of
1109 *Drosophila melanogaster* strain w1118; iso-2; iso-3. *Fly (Austin)* **6**, 80-92,
1110 doi:10.4161/fly.19695 (2012).
1111 33 Li, H. Minimap2: pairwise alignment for nucleotide sequences.
1112 *Bioinformatics* **34**, 3094-3100, doi:10.1093/bioinformatics/bty191 (2018).
1113 34 Capella-Gutierrez, S., Silla-Martinez, J. M. & Gabaldon, T. trimAl: a tool
1114 for automated alignment trimming in large-scale phylogenetic analyses.
1115 *Bioinformatics* **25**, 1972-1973, doi:10.1093/bioinformatics/btp348 (2009).
1116 35 Stamatakis, A. RAxML version 8: a tool for phylogenetic analysis and
1117 post-analysis of large phylogenies. *Bioinformatics* **30**, 1312-1313,
1118 doi:10.1093/bioinformatics/btu033 (2014).
1119 36 Bouckaert, R. *et al.* BEAST 2: a software platform for Bayesian
1120 evolutionary analysis. *PLoS Comput Biol* **10**, e1003537,
1121 doi:10.1371/journal.pcbi.1003537 (2014).
1122 37 Hasegawa, M., Kishino, H. & Yano, T. Dating of the human-ape splitting
1123 by a molecular clock of mitochondrial DNA. *J Mol Evol* **22**, 160-174,
1124 doi:10.1007/BF02101694 (1985).
1125 38 Vohringer, H. S. *et al.* Genomic reconstruction of the SARS-CoV-2
1126 epidemic in England. *Nature* **600**, 506-511,
1127 doi:10.1038/s41586-021-04069-y (2021).
1128 39 Obermeyer, F. *et al.* Analysis of 2.1 million SARS-CoV-2 genomes
1129 identifies mutations associated with transmissibility. *MedRxiv*, doi:
1130 <https://doi.org/10.1101/2021.1109.1107.21263228> (2022).
1131 40 Yamamoto, M. *et al.* The Anticoagulant Nafamostat Potently Inhibits
1132 SARS-CoV-2 S Protein-Mediated Fusion in a Cell Fusion Assay System
1133 and Viral Infection In Vitro in a Cell-Type-Dependent Manner. *Viruses* **12**,
1134 doi:10.3390/v12060629 (2020).

1135 41 Ozono, S. *et al.* SARS-CoV-2 D614G spike mutation increases entry
1136 efficiency with enhanced ACE2-binding affinity. *Nat Commun* **12**, 848,
1137 doi:10.1038/s41467-021-21118-2 (2021).

1138 42 Liu, Y. *et al.* The SARS-CoV-2 Delta variant is poised to acquire complete
1139 resistance to wild-type spike vaccines. *BioRxiv*, doi:
1140 <https://doi.org/10.1101/2021.1108.1122.457114> (2021).

1141 43 Uriu, K. *et al.* Neutralization of the SARS-CoV-2 Mu Variant by
1142 Convalescent and Vaccine Serum. *N Engl J Med* **385**, 2397-2399,
1143 doi:10.1056/NEJMc2114706 (2021).

1144 44 Ozono, S., Zhang, Y., Tobiume, M., Kishigami, S. & Tokunaga, K.
1145 Super-rapid quantitation of the production of HIV-1 harboring a
1146 luminescent peptide tag. *J Biol Chem* **295**, 13023-13030,
1147 doi:10.1074/jbc.RA120.013887 (2020).

1148 45 Reed, L. J. & Muench, H. A Simple Method of Estimating Fifty Percent
1149 Endpoints. *Am J Hygiene* **27**, 493-497 (1938).

1150 46 Zahradnik, J. *et al.* A Protein-Engineered, Enhanced Yeast Display
1151 Platform for Rapid Evolution of Challenging Targets. *ACS Synth Biol* **10**,
1152 3445-3460, doi:10.1021/acssynbio.1c00395 (2021).

1153 47 Zahradnik, J. *et al.* SARS-CoV-2 variant prediction and antiviral drug
1154 design are enabled by RBD in vitro evolution. *Nat Microbiol* **6**, 1188-1198,
1155 doi:10.1038/s41564-021-00954-4 (2021).

1156 48 Peleg, Y. & Unger, T. Application of the restriction-free (RF) cloning for
1157 multicomponents assembly. *Methods Mol Biol* **1116**, 73-87,
1158 doi:10.1007/978-1-62703-764-8_6 (2014).

1159
1160

Author Contributions

Daichi Yamasoba, Izumi Kimura, Hesham Nasser, Keiya Uriu, Kotaro Shirakawa, Yusuke Kosugi, Mako Toyoda, Yuri L Tanaka, Erika P Butlertanaka, Ryo Shimizu, Kayoko Nagata, Takamasa Ueno, Akatsuki Saito, Takashi Irie, Terumasa Ikeda, Kei Sato performed cell culture experiments.

Jiri Zahradnik, Gideon Schreiber performed an yeast surface display assay.

Yuhei Morioka, Naganori Nao, Rigel Suzuki, Mai Kishimoto, Kouji Kobiyama, Teppei Hara, Hayato Ito, Yasuko Orba, Michihito Sasaki, Kumiko Yoshimatsu, Ken J Ishii, Hirofumi Sawa, Keita Matsuno, Takasuke Fukuhara performed animal experiments.

Masumi Tsuda, Lei Wang, Yoshitaka Oda, Shinya Tanaka performed histopathological analysis.

Hirofumi Asakura, Mami Nagashima, Kenji Sadamasu, Kazuhisa Yoshimura performed viral genome sequencing analysis.

Kotaro Shirakawa, Jin Kuramochi, Motoaki Seki, Ryoji Fujiki, Atsushi Kaneda, Tadanaga Shimada, Taka-aki Nakada, Seiichiro Sakao, Takuji Suzuki, Akifumi Takaori-Kondo contributed clinical sample collection.

Jumpei Ito performed statistical, modelling, and bioinformatics analyses.

Jumpei Ito, Akatsuki Saito, Takashi Irie, Shinya Tanaka, Keita Matsuno, Takasuke Fukuhara, Terumasa Ikeda, and Kei Sato designed the experiments and interpreted the results.

Jumpei Ito and Kei Sato wrote the original manuscript.

All authors reviewed and proofread the manuscript.

The Genotype to Phenotype Japan (G2P-Japan) Consortium contributed to the project administration.

Conflict of interest

The authors declare that no competing interests exist.

Acknowledgments

We would like to thank all members belonging to The Genotype to Phenotype Japan (G2P-Japan) Consortium. We thank Dr. Kenzo Tokunaga (National Institute for Infectious Diseases, Japan) and Dr. Jin Gohda (The University of Tokyo, Japan) and Dr. Hisashi Arase (Osaka University) for providing reagents. The super-computing resource was provided by Human Genome Center at The University of Tokyo.

This study was supported in part by AMED Research Program on Emerging and Re-emerging Infectious Diseases (20fk0108268, to Akifumi Takaori-Kondo; 20fk0108517, to Akifumi Takaori-Kondo; 20fk0108401, to Takasuke Fukuhara; 20fk010847, to Takasuke Fukuhara; 21fk0108617 to Takasuke Fukuhara; 20fk0108146, to Kei Sato; 20fk0108270, to Kei Sato; and

20fk0108413, to Atsushi Kaneda, Terumasa Ikeda and Kei Sato) and (20fk0108451, to G2P-Japan Consortium, Akatsuki Saito, Takashi Irie, Keita Matsuno, Takasuke Fukuhara, Terumasa Ikeda, and Kei Sato); AMED Research Program on HIV/AIDS (21fk0410034, to Akifumi Takaori-Kondo; 21fk0410033, to Akatsuki Saito; and 21fk0410039, to Kei Sato); AMED CRDF Global Grant (21jk0210039 to Akatsuki Saito); AMED Japan Program for Infectious Diseases Research and Infrastructure (21wm0325009, to Akatsuki Saito; 21wm0125008, to Hirofumi Sawa and 21wm0225003, to Hirofumi Sawa); JST A-STEP (JPMJTM20SL, to Terumasa Ikeda); JST SICORP (e-ASIA) (JPMJSC20U1, to Kei Sato); JST SICORP (JPMJSC21U5, to Kei Sato), JST CREST (JPMJCR20H4, to Kei Sato); JSPS KAKENHI Grant-in-Aid for Scientific Research C (19K06382, to Akatsuki Saito); JSPS KAKENHI Grant-in-Aid for Scientific Research B (21H02736, to Takasuke Fukuhara; 18H02662, to Kei Sato; and 21H02737, to Kei Sato); JSPS Fund for the Promotion of Joint International Research (Fostering Joint International Research) (18KK0447, to Kei Sato); JSPS Core-to-Core Program (A. Advanced Research Networks) (JPJSCCA20190008, to Kei Sato); JSPS Research Fellow DC1 (19J20488, to Izumi Kimura); JSPS Leading Initiative for Excellent Young Researchers (LEADER) (to Terumasa Ikeda); World-leading Innovative and Smart Education (WISE) Program 1801 from the Ministry of Education, Culture, Sports, Science and Technology (MEXT) (to Naganori Nao); The Tokyo Biochemical Research Foundation (to Kei Sato); Mitsubishi Foundation (to Terumasa Ikeda); Shin-Nihon Foundation of Advanced Medical Research (to Mako Toyoda and Terumasa Ikeda); Tsuchiya Foundation (to Takashi Irie); a Grant for Joint Research Projects of the Research Institute for Microbial Diseases, Osaka University (to Akatsuki Saito); an intramural grant from Kumamoto University COVID-19 Research Projects (AMABIE) (to Terumasa Ikeda); Intercontinental Research and Educational Platform Aiming for Eradication of HIV/AIDS (to Terumasa Ikeda); and Joint Usage/Research Center program of Institute for Frontier Life and Medical Sciences, Kyoto University (to Kei Sato).

1232

1233 **Consortia**

1234 **The Genotype to Phenotype Japan (G2P-Japan) Consortium**

1235 Mai Suganami¹, Akiko Oide¹, Mika Chiba¹, Tomokazu Tamura⁵, Kana Tsushima⁵,
1236 Haruko Kubo⁵, Zannatul Ferdous⁹, Hiromi Mouri⁹, Miki Iida⁹, Keiko Kasahara⁹,
1237 Koshiro Tabata⁹, Mariko Ishizuka⁹, Asako Shigeno²⁹, Kenzo Tokunaga³², Seiya
1238 Ozono³², Isao Yoshida²¹, So Nakagawa³³, Jiaqi Wu³³, Miyoko Takahashi³³,
1239 Bahityar Rahmutulla Nawai²³, Yutaka Suzuki³⁴, Yukie Kashima³⁴, Kazumi Abe³⁴,
1240 Kiyomi Imamura³⁴, Ryoko Kawabata²⁸, Otowa Takahashi³, Kimiko Ichihara³,
1241 Kazuko Kitazato³, Haruyo Hasebe³, Chihiro Motozono¹⁷, Toong Seng Tan¹⁷,
1242 Isaac Ngare¹⁷

1243

1244 ³² National Institute of Infectious Diseases, Tokyo, Japan

1245 ³³ Tokai University, Isehara, Japan

1246 ³⁴ The University of Tokyo, Kashiwa, Japan

1247

Figure legends

Fig. 1 | Epidemic of BA.2.

a, Maximum likelihood tree of the Omicron lineages sampled from South Africa. Asterisk denote nodes with ≥ 0.95 bootstrap values. **b**, Number of amino acid differences between viral lineages detected in S (filled) or the other regions (opened). **c**, Relative frequency of BA.2 in the genome surveillance data during January 2022. The values for the countries with ≥ 20 SARS-CoV-2 sequences are shown. **d**, Estimated relative effective reproduction number of each viral lineage, assuming a fixed generation time of 2.1 days. The global average value estimated by a Bayesian hierarchical model is shown. The value in each country is shown in **Extended Data Fig. 2d**. The posterior distribution (violin), 95% CI (line), and posterior mean (dot) are shown.

Fig. 2 | Immune resistance of BA.2.

a, Amino acid substitutions in S. Left, primary structure and respective domains. Numbers indicate amino acid position. NTD, N-terminal domain; RBM, receptor-binding motif; HR, heptad repeat; TMD, transmembrane domain. Right, heatmap showing the frequency of amino acid substitutions. Substitutions detected in $>10\%$ sequences of any lineages are shown. **b–h**, Neutralisation assays. Neutralisation assays were performed with the pseudoviruses harbouring the S proteins of B.1.1 (the D614G-bearing ancestral virus), Delta, BA.1 and BA.2. Vaccinated sera [**b**, mRNA-1273 (16 donors); **c**, ChAdOx1 (9 donors)], monoclonal antibodies (**d**), convalescent sera of the individuals infected with early pandemic virus (until May 2020) (**e**, 12 donors), and BA.1 (**f**, 17 donors), convalescent sera of the hamsters infected B.1.1 (**g**, left; 6 hamsters) and BA.1 (**g**, right; 6 hamsters), and murine sera immunised with the cells expressing B.1.1 S (**h**, left; 10 mice) and BA.1 S (**h**, right; 10 mice) were used. In **b,c,e–h**, assay of each serum was performed in triplicate to determine 50% neutralisation titre (NT50). Each dot represents each NT50 value, and geometric mean and 95% CI are shown. Number indicates the fold change of resistance versus each antigenic variant. Statistically significant differences between BA.1 and BA.2 were determined by two-sided Wilcoxon signed-rank test. Information of vaccinated/convalescent donors are summarized in **Supplementary Tables 1 and 2**. In **f**, the dots of not-fully vaccinated 4 donors are filled. In **d**, assay of each concentration was performed in triplicate, and data are the average \pm s.d. IC50, 50% inhibitory concentration; ND, not determined.

Fig. 3 | Virological features of BA.2 in vitro.

a,h, Growth kinetics of SARS-CoV-2 variants. **b**, Fluorescence microscopy. GFP area of infected VeroE6/TMPRSS2 cells at 48 h.p.i were measured. Numbers in

the panel indicate the number of GFP-positive cells counted. **c**, Plaque assay. Diameter of plaques (20 plaques per virus) are summarized. **d,f**, S-based fusion assay. The fusion activity (arbitrary units) is shown. **e**, Western blot. Left, representative blots of S-expressing cells. ACTB is an internal control. Right, the ratio of S2 to the full-length S plus S2 proteins. **g**, Fold increase of pseudovirus infectivity by TMPRSS2 expression. Assays were performed in quadruplicate (**a,g,h**), octuplicate (**a**, most left) or triplicate (**d–f**) and data are the average \pm s.d. Each dot indicates the result from an individual plaque (**c**) and an individual replicate (**e,g**). In **b** and **c**, raw data are shown in **Extended Data Fig. 5 and 6**. Statistically significant differences between BA.2 and other variants through timepoints were determined by multiple regression (**a,d,f,h**). Familywise error rates (FWERs) calculated using the Holm method are indicated in the figures. Statistically significant differences between BA.1 and BA.2 were determined by two-sided Mann–Whitney *U*-tests (**b,d**) or two-sided paired Student's *t*-tests (**e**).

Fig. 4 | Virological features of BA.2 in vivo.

Syrian hamsters were intranasally inoculated with B.1.1, BA.1 and BA.2. **a**, Body weight, Penh, Rpef, SpO₂ values routinely measured. Hamsters of the same age were intranasally inoculated with PBS (uninfected). **b**, Viral RNA load in the lung hilum (left) and periphery (right). **c,d**, Percentage of N-positive cells in the whole lobes of lung (**c**) and bronchiole in the frontal/upper lobe of lung (**d**) measured by IHC. **e**, Histopathological scoring of lung lesions. Representative pathological features are shown in our previous studies^{12,23}. Data are the average (**a**, 6 hamsters per each group; **b–e**, 4 hamsters per each group) \pm s.e.m. In **a–c,e**, statistically significant differences between BA.2 and other variants or uninfected hamsters through timepoints were determined by multiple regression. The data at 0 d.p.i. was excluded from the analyses. FWERs calculated using the Holm method are indicated in the figures. In **d**, each dot indicates the result from an individual hamster. In **c–e**, raw data are shown in **Extended Data Fig. 7 and 8**.

1318 **Extended Data**

1319

1320 **Extended Data Fig. 1. Estimated emergence dates of the Omicron lineages.**

1321 **a**, Phylodynamics of BA.1 (top), BA.2 (middle), and BA.3 (bottom) sampled by
1322 January 26, 2022 in South Africa. All the BA.2 and BA.3 sequences and 200
1323 randomly sampled BA.1 (including 20 BA.1.1) sequences were used. The
1324 time-resolved trees were constructed by BEAST2. Regarding a node with ≥ 0.95
1325 posterior value (denoted by an asterisk), the 95% CI of the divergence time is
1326 shown. **b**, Estimated emergence dates of the Omicron lineages. The 95% CI
1327 (error bar) and posterior mean (dot) are shown.

1328

1329 **Extended Data Fig. 2. Epidemic dynamics of SARS-CoV-2 lineages in** 1330 **countries with the BA.2 epidemic.**

1331 **a**, Daily sequence frequency of each viral lineage in eleven countries where
1332 ≥ 100 BA.2 sequences have been reported by January 25, 2022. This data was
1333 used as an input of a Bayesian hierarchical model to estimate the epidemic
1334 dynamics.

1335 **b,c**, Epidemic dynamics of SARS-CoV-2 viral lineages. The observed daily
1336 frequency (dot) and the dynamics estimated by the Bayesian model (posterior
1337 mean; line) are shown. Additionally, 95% CI (**b**) and 90% prediction interval (**c**)
1338 are shown. **d**, Estimated relative effective reproduction number of each viral
1339 lineage in each country. The posterior distribution (violin), 95% CI (line), and
1340 posterior mean (dot) are shown.

1341

1342 **Extended Data Fig. 3. Immune resistance of BA.2.**

1343 Neutralisation assays were performed with the pseudoviruses harbouring the S
1344 proteins of B.1.1 (the D614G-bearing ancestral virus), Alpha, Delta, BA.1 and
1345 BA.2. Assay of each serum sample was performed in triplicate to determine
1346 NT50, and each dot represents each NT50 value. Geometric mean and 95% CI
1347 are shown. The number indicates the fold change of resistance versus each
1348 antigenic variant. In **a** and **b**, statistically significant differences between BA.1
1349 and BA.2 were determined by two-sided Wilcoxon signed-rank test. In **c**,
1350 statistically significant differences between fully-vaccinated (13 donors) and
1351 not-fully-vaccinated (4 donors) were determined by two-sided Mann-Whitney
1352 U-test. Information of vaccinated and convalescent donors are summarized in
1353 **Supplementary Tables 1 and 2**, respectively.

1354

1355 **Extended Data Fig. 4. Scheme of chimeric recombinant SARS-CoV-2 used** 1356 **in this study.**

1357 The SARS-CoV-2 genome and respective genes are shown. The template is
1358 SARS-CoV-2 strain WK-521 (lineage A, GISAID ID: EPI_ISL_408667), and the

1359 S genes were swapped with respective lineage/strain (GISAID IDs are indicated
1360 in the figure). Additionally, the *ORF7b* was swapped with *sfGFP* gene.

1361

1362 **Extended Data Fig. 5. Syncytia and plaque formations by BA.2.**

1363 **a**, Fluorescence microscopy. GFP area of infected VeroE6/TMPRSS2 cells
1364 (m.o.i. 0.01) at 24, 48, and 72 h.p.i were measured. Higher-magnification views
1365 of the regions indicated by squares are shown at bottom. **b**, Plaque assay. **c**,
1366 Coculture of S-expressing cells with HEK293-ACE2/TMPRSS2 cells. Left,
1367 representative images of S-expressing cells cocultured with HEK293 cells (top)
1368 or HEK293-ACE2/TMPRSS2 cells (bottom). Nuclei were stained with Hoechst
1369 33342 (blue). Right, the size distribution of syncytia (green). Numbers in the
1370 panel indicate the numbers of GFP-positive syncytia counted. Data are the
1371 average \pm s.d. A statistically significant difference between BA.1 and BA.2 was
1372 determined by two-sided Mann–Whitney *U*-test. In **a** and **b**, summarized data
1373 are shown in **Fig. 3b** and **3c**. Scale bars, 500 μ m (**a**) or 200 μ m (**c**).

1374

1375 **Extended Data Fig. 6. Expression and binding properties of BA.2 S.**

1376 **a**, S expression on the cell surface. Representative histograms stained with
1377 anti-S1/S2 polyclonal antibody (left) and the summarised data (right) are
1378 respectively shown. The number in the histogram indicates MFI. Grey
1379 histograms indicate isotype controls. **b**, Binding affinity of SARS-CoV-2 S RBD
1380 to ACE2 by yeast surface display. Left, The percentage of the binding of the
1381 SARS-CoV-2 S RBD expressed on yeast to soluble ACE2 (left) and the
1382 summarised data (right) are respectively shown. **c**, TMPRSS2 expression on the
1383 cell surface. Left, representative histograms stained with anti-TMPRSS2
1384 polyclonal antibody are shown. The number in the histogram indicates MFI. Grey
1385 histograms indicate isotype controls. Right, summarized data. Assays were
1386 performed in triplicate, and data are the average \pm s.d. Each dot indicates the
1387 result from an individual replicate. A statistically significant difference between
1388 BA.1 and BA.2 was determined by two-sided unpaired Student's *t*-test (**a**) or
1389 two-sided Mann–Whitney *U*-test (**b**).

1390

1391 **Extended Data Fig. 7. IHC of SARS-CoV-2 N protein.**

1392 **a,b**, IHC of viral N protein in the middle part of trachea of all infected hamsters (*n*
1393 = 4 per each viral strain) at 1 d.p.i. (**a**) and the lung at 1, 3 and 5 d.p.i. (**b**). Each
1394 panel indicates the representative result from an individual infected hamster. **c**,
1395 Lung lobes of the hamsters infected with B.1.1, BA.1 or BA.2 (*n* = 4 for each
1396 virus) at 1, 3 and 5 d.p.i. were immunohistochemically stained with
1397 anti-SARS-CoV-2 N monoclonal antibody. In each panel, IHC staining (top) and
1398 the digitalized N-positive area (bottom, indicated in red) are shown. The number

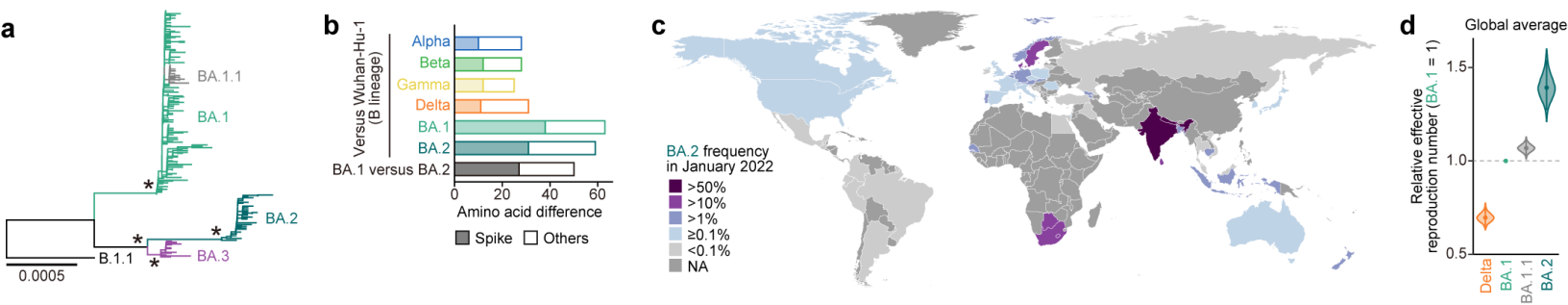
1399 in the bottom panel indicates the percentage of N-positive area. Summarized
1400 data is shown in **Fig. 4c**. Scale bars, 1 mm (**a**); 500 μ m (**b**); or 5 mm (**c**).

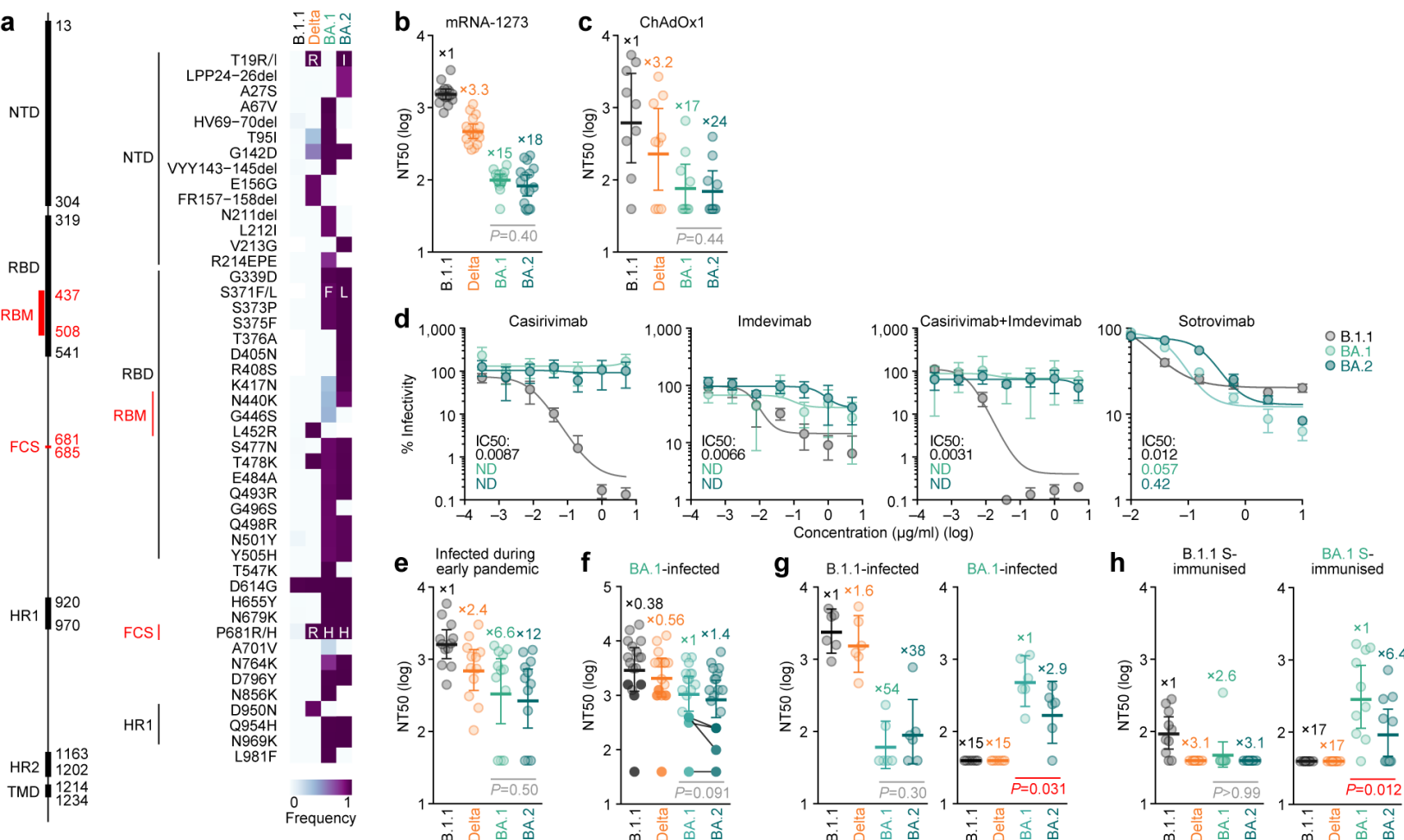
1401

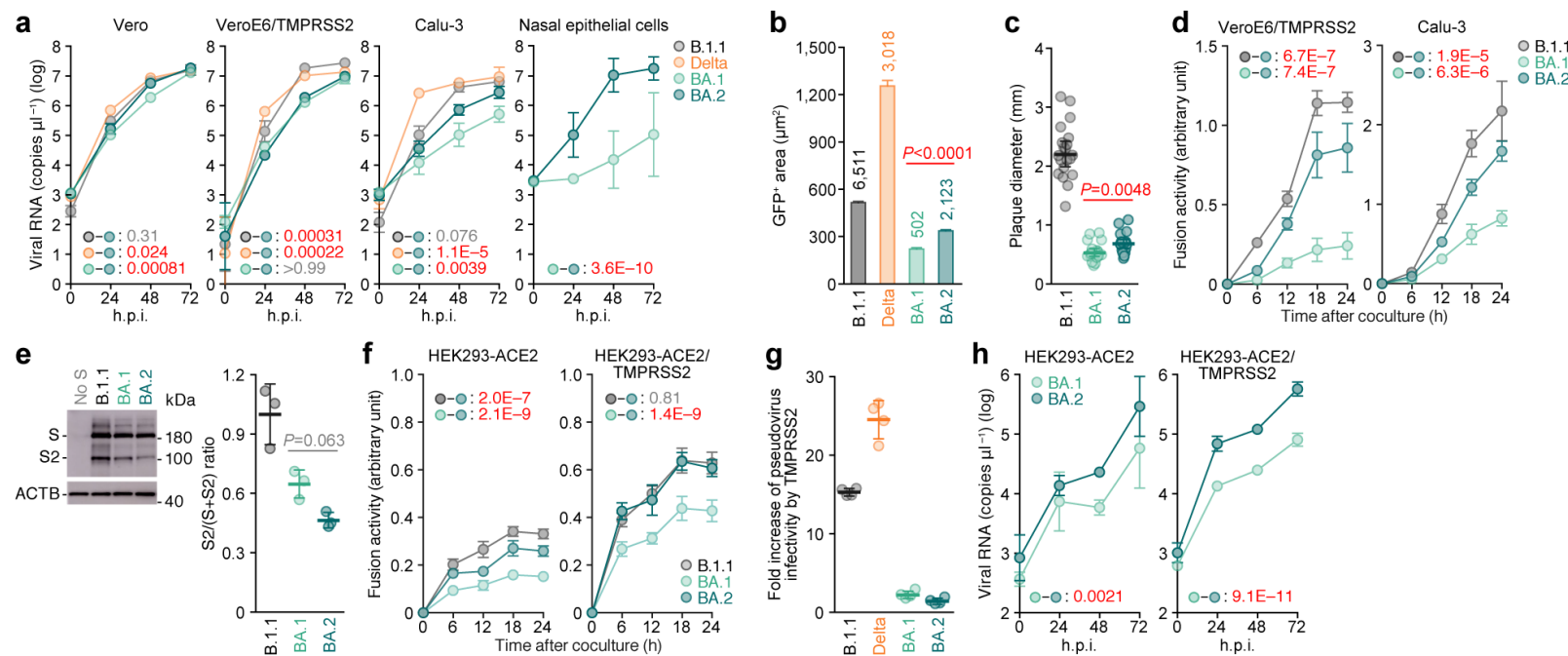
1402 **Extended Data Fig. 8. Pathological features of BA.2.**

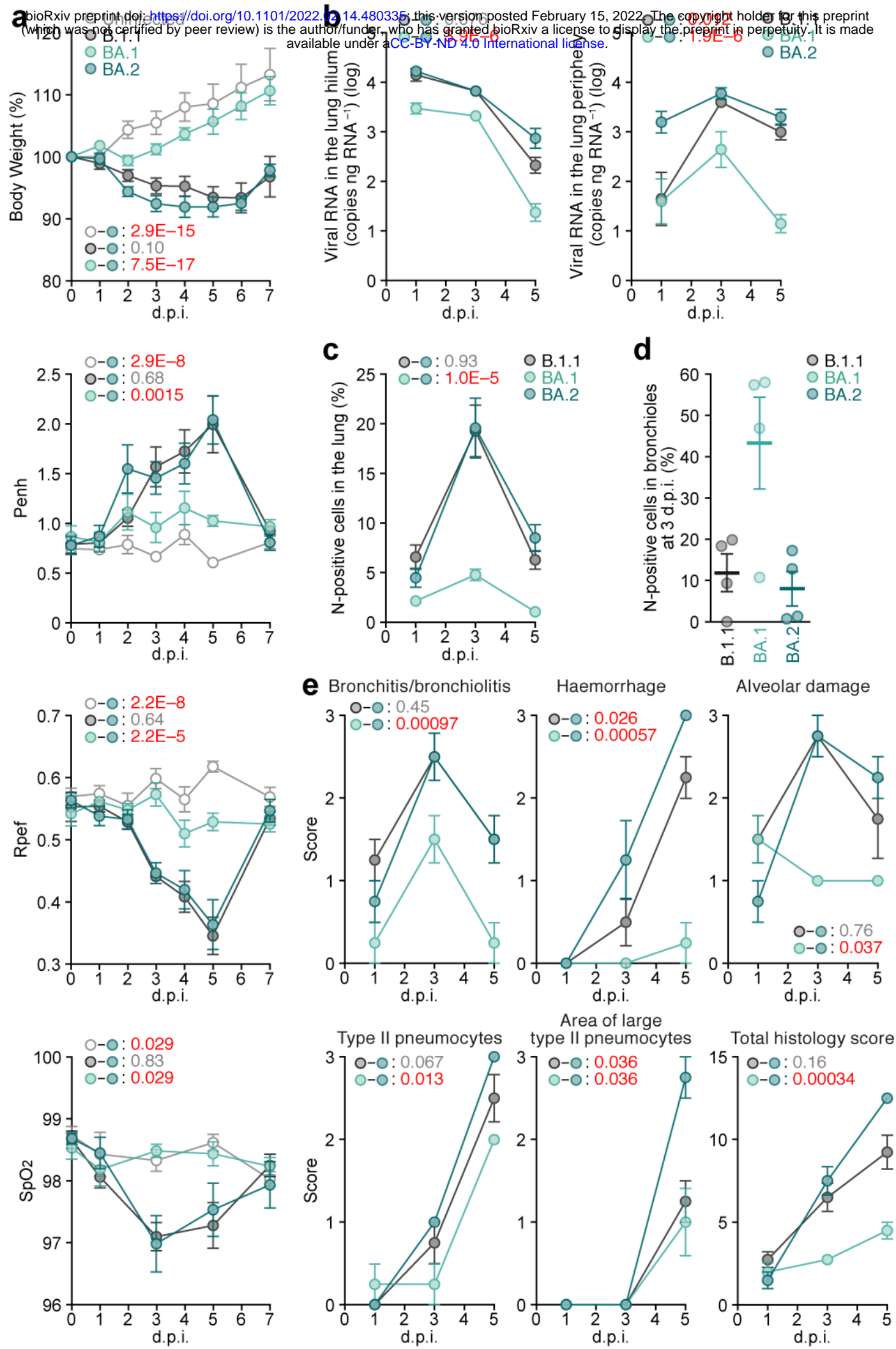
1403 **a**, H&E staining of the lungs of infected hamsters. Uninfected lung alveolar
1404 space and bronchioles are also shown. **b**, Type II pneumocytes in the lungs of
1405 infected hamsters. Left, lung lobes of the hamsters infected with B.1.1 (n = 4),
1406 BA.1 (n = 4), and BA.2 (n = 4) at 5 d.p.i. In each panel, H&E staining (top) and
1407 the digitalized inflammation area (bottom, indicated in red) are shown. The
1408 number in the bottom panel indicates the percentage of the section represented
1409 by the indicated area (i.e., the area indicated with red colour per the total area of
1410 the lung lobes). Right, summarized data. Each dot indicates the result from an
1411 individual hamster.

1412 Scale bars, 250 μ m (**a**) or 5 mm (**b**).



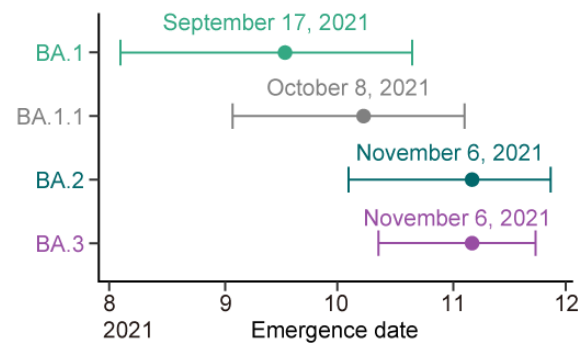
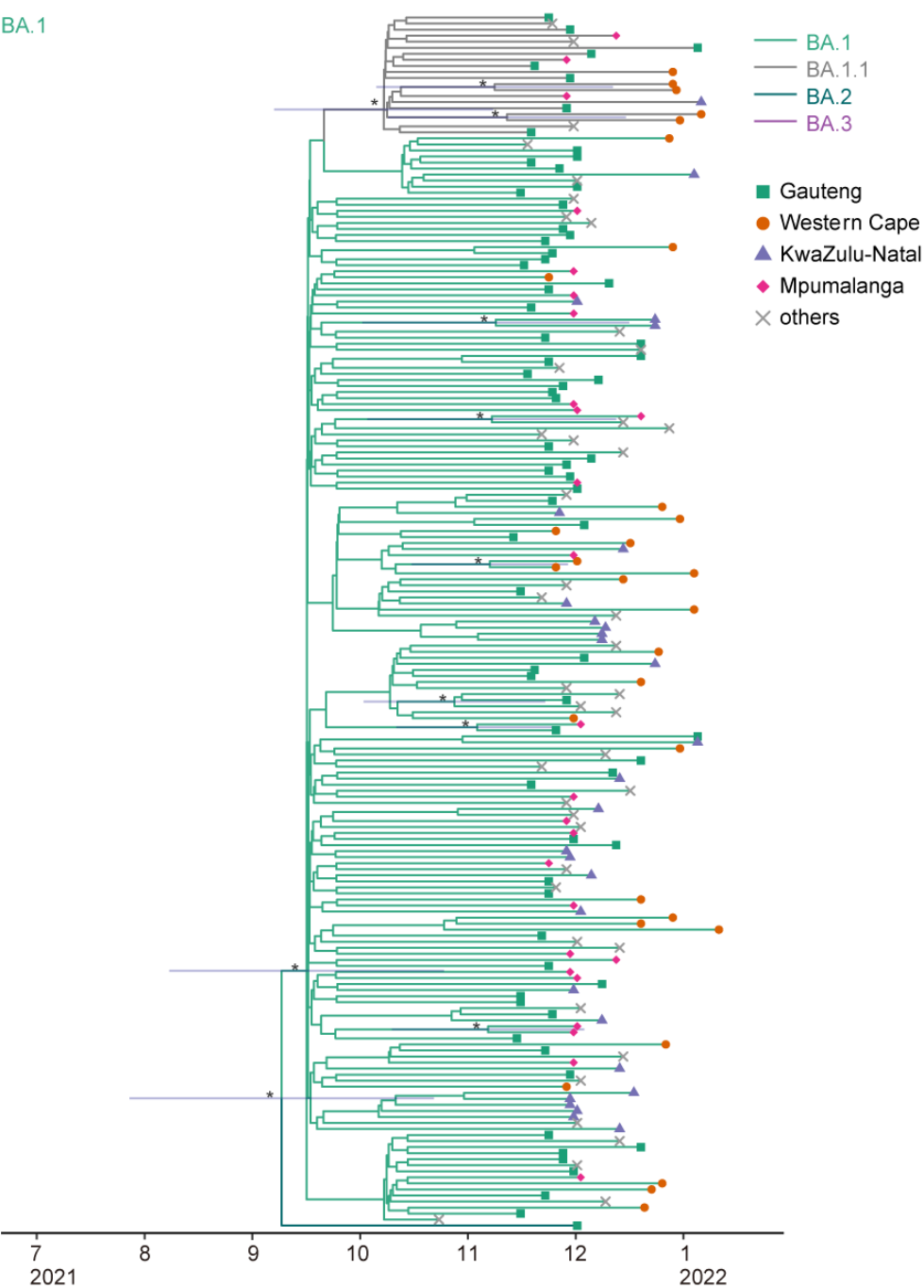




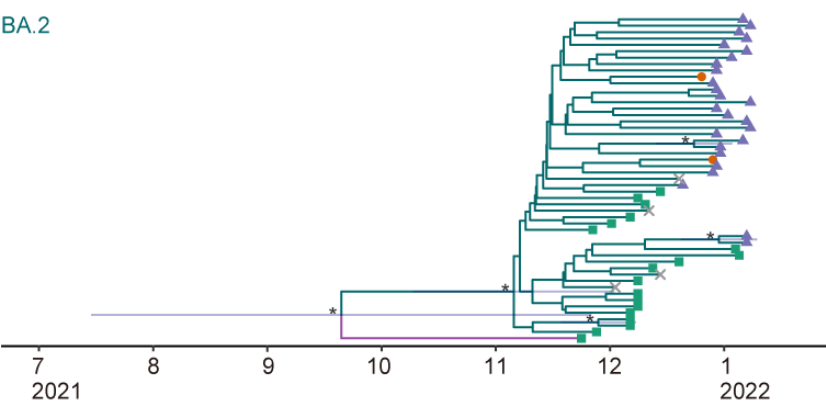


a

BA.1



BA.2



BA.3

